Energy & Environmental Science

Accepted Manuscript

ROYAL SOCIETY OF CHEMISTRY

www.rsc.org/ees

Energy & Environmental Science RSCPublishing

Review

Planar Heterojunction Organometal Halide Perovskite Solar Cells: Role of Interfacial Layers

Cite this: DOI: 10.1039/x0xx00000x

Hobeom Kim†, Kyung-Geun Lim†, Tae-Woo Lee*

Received 00th January 2015,
Accepted 00th January 2015

DOI: 10.1039/x0xx00000x

www.rsc.org/

Organometal halide perovskites are promising photo-absorption materials in solar cells due to high extinction coefficient, broad light absorption range and excellent semiconducting properties. The highest power conversion efficiency (PCE) of perovskite solar cells (PrSCs) is now 20.1%. However, a high-temperature processed mesoscopic metal oxide (e.g., TiO_2) must be removed to realize flexible PrSCs on plastic substrates using low temperature processes. Although the planar heterojunction (PHJ) structure can be considered as the most appropriate structure for flexible PrSCs, they have shown lower PCEs than those with a mesoscopic metal oxide layer. Therefore, development of interfacial layers is essential for achieving highly efficient PHJ PrSCs, and necessary in fabrication of flexible PrSCs. This review article gives an overview of progress in PHJ PrSCs and the roles of interfacial layers in the device, and suggests a practical strategy to fabricate highly efficient and flexible PHJ PrSCs. We conclude with our technical suggestion and outlook for further research direction.

1. Introduction

Organometal metal halide perovskites are promising materials for various optoelectronic and photonic devices including solar cells,[1–4] light-emitting diodes,[5–7] photodiodes.[8–10] Furthermore, low threshold lasing has been reported from this material.[11–13] Active research based on organic-inorganic hybrid perovskite has focused on perovskite solar cells (PrSCs) because of the recent rapid achievements in increasing their power conversion efficiency (PCE): the first liquid-junction PrSCs were reported in 2009[14] and PCEs of solid-state PrSCs reached 20.1 % in 2015.[4]

This rapid increase in PCE has been achieved mainly by improving device architecture and fabrication techniques. In addition to high PCE, PrSCs have two great advantages. (1) Organic-inorganic hybrid perovskite has a high absorption coefficient, so a thin (<500 nm) film of perovskite light absorber is sufficient as a photo-active layer in PrSCs. Therefore, the device can be thin and light. (2) With these features, flexible, large-area PrSCs can be fabricated at low cost. Because of these advantages and high PCE, PrSCs have the potential to replace conventional Si solar cells, and to provide portable, mobile, and wearable power sources.

PrSCs inherited the architecture of dye-sensitized solar cells (DSSCs),[15–17] most of which include a mesoscopic metal oxide layer (e.g., TiO_2), so the structure of early-stage PrSCs was similar to those of DSSCs,[14,18] and many studies still present mesoscopic PrSCs with very high PCEs. However, this type of PrSC cannot be developed as a flexible device because formation of mesoporous structure requires high temperature T > 450 °C, which damages most flexible plastic substrates. Also, the high-T processes for development of mesoscopic PrSCs makes it difficult to complete tandem structure which is a promising configuration for increasing PCE of solar cells, but needs low-T processable interconnecting layer between bottom and upper cells to avoid destruction of layers underneath it.

Instead, use of planar heterojunction (PHJ) PrSCs that include low-T processable interlayers without mesoscopic structure can provide a method to fabricate flexible PrSCs and tandem PrSCs. Furthermore, nonuse of mesoscopic structure simplifies the structure of PrSCs and reduces the cost and time for fabrication. Theoretical and experimental research on PHJ PrSCs has led to PCE > 19 %.[19] Many studies on PHJ PrSCs to date have focused on engineering of perovskite film as a photo-active layer to make it favourable to solar cells,[20–46] but studies on interlayer engineering of PrSCs are relatively lacking. A PHJ PrSC with high open circuit voltage V_{oc}, high short circuit current J_{sc}, and high fill factor FF can be achieved by using appropriate interfacial layers between electrodes and perovskite light absorber. Basically, to maximize built-in potential of the device and to facilitate charge transfer from perovskite to interfacial layers, the PHJ PrSC should use a hole extraction layer (HEL) and an electron extraction layer (EEL) with a well-matching ionization energy (IE) and electron affinity (EA) respectively to those of perovskites.[47–49] Also, use of interfacial

layers with high electrical conductivity are favourable to make efficient charge transport and extraction to each electrode.

The defect chemistry of perovskite is another topic of study. Traps in perovskite film and at the interface between perovskite and interfacial layer have a strong influence on photophysical and photoelectrical properties of devices and thereby on device performance. High density of the trap states results in non-radiative recombination which is an undesirable physical process in PrSCs that leads to hysteresis behaviour, depending on photocurrent measurement condition.[50–54] For these reasons, to improve the performance of PHJ PrSCs, the interfacial layers between electrodes and perovskite absorber must be engineered appropriately.

In this review, we focus on the development of PHJ PrSCs which have a strong potential to be applied to flexible devices, and especially focus on work about interfacial layer engineering. Sections 2 and 3 provide basic explanations of structural and physical properties of perovskite and on progress in PrSCs, particularly those of the PHJ type. Section 4 reviews the functions of interfacial layer in PHJ PrSCs. Section 5 reviews research on flexible PHJ PrSCs. Section 6 presents conclusions.

2. Principles of organic-inorganic perovskite materials

Perovskite is a crystal structure that originated from a calcium titanium oxide mineral ($CaTiO_3$). Generally, perovskite has an ABX_3 formula, where cation A is located at the corner positions (0,0,0), cation B is at the centre (1/2,1/2,1/2) and monovalent anion X is at the centre of the six planes (1/2,1/2,0) assuming it is in the idealized cubic unit cell (Fig. 1). The most widely-used component materials of perovskites for PrSCs are organic molecule cations based on amine at A sites (e.g., $C_nH_{2n+1}NH_3^+$, $HC(NH_2)_2^+$), metal cations (e.g., Pb^{2+}, Sn^{2+}, Cu^{2+}) at B sites, and halide anions (Cl^-, Br^-, I^-) at X sites. Various kinds of organic-inorganic hybrid perovskite are based on the configuration that Mitzi *et al*. formulated by incorporating an organic modulation layer between metal halide sheets.[55] The formation of perovskite structure can be estimated by tolerance factor[56]

$$t = \frac{R_A + R_B}{\sqrt{2}(R_B + R_X)}$$

and octahedral factor

$$\mu = R_B/R_X,$$

where R_A, R_B, and R_X are the effective ionic radii of A, B, and X, respectively. Perovskite structure is stable when $0.813 \leq t \leq 1.107$ and $0.442 \leq \mu \leq 0.895$.[57]

Some perovskites (e.g., $MAPbI_3$, $MAPbI_xCl_{3-x}$ and $FAPbI_3$ [MA: Methylammonium CH_3NH_3, FA: Formamidinium $HC(NH_2)_2$]) have broad absorption spectra with suitable band gap ~1.5 – 1.6 eV, therefore some are used as light absorbers in PrSCs. In addition to absorption spectra, a perovskite that is

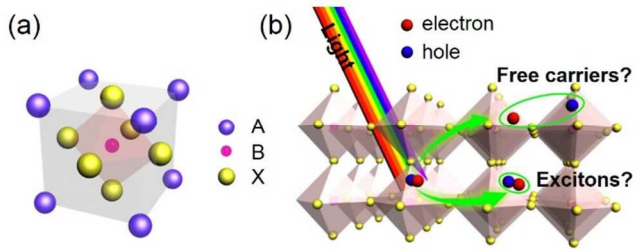

Fig. 1 (a) Crystal structure of organic-inorganic perovskite. (b) What is the generated species, free carriers or excitons after photo-excitation of perovskite.

suitable as light harvester in PrSCs should have appropriate dielectric constant ε, exciton binding energy E_b, Bohr radius, and diffusion length of charge carriers. These factors have a strong relation to photophysical, photoelectrical properties and solar cell device performance. The photo-generated electron-hole pairs in these organic-inorganic perovskites can exist as free charge carriers or excitons with E_b, and the excitons can be classified as Frenkel-type or Wannier-type depending on the perovskites's E_b. Many researchers have reported that the comparable E_b of perovskite materials (29–50 meV for $MAPbI_3$,[58–61] 35–98 meV for $MAPbCl_{3-x}I_x$[62,63]) to thermal energy (~25 meV) at room temperature facilitates exciton dissociation. Recently, there was a report that $MAPbI_3$ has E_b of 2 meV which is very low compared to inorganic semiconductors (e.g., Si, 15.0 meV; GaAs, 4.2 meV; CdTe, 10.5 meV).[64] Although what species are generated under illumination and what is the make-up of the species in perovskite materials are still under debate, free carriers easily dissociated from excitons contribute to ambipolar charge transport in the materials.[65,66] Based on these excellent capabilities of light absorption and photophysical/photoelectrical properties, perovskites are considered as promising materials for solar cell devices.

3. Progress in perovskite solar cells

3.1. Mesoscopic vs. Planar

Miyasaka *et al*. (2009) developed the first PrSCs; the devices had a perovskite photosensitizer but otherwise had nearly identical structural configuration to conventional DSSCs.[14] The structure of devices was $TiCl_4$ treated fluorine-doped tin oxide (FTO) (anode)/mesoporous TiO_2/perovskite sensitizer/Pt-coated FTO (cathode); the gap between the electrodes was filled with liquid electrolyte. With this structure, PCEs of devices using $MAPbBr_3$ and $MAPbI_3$ were 3.13 % and 3.81 % respectively. Subsequent research by Park *et al*. (2011) used the initial liquid-junction device configuration and achieved improved PCE = 6.5 %, but the liquid electrolyte dissolved the perovskite crystal, so stability of the device could not be guaranteed.[18] This problem was solved by using a solid-state hole conductor, spiro-OMeTAD, on top of perovskite layer instead of using liquid electrolyte[1]; the resulting device showed long-term stability for over 500 h and PCE > 9 % (Fig. 2a-e). Grätzel *et al*. (2013) introduced a sequential deposition

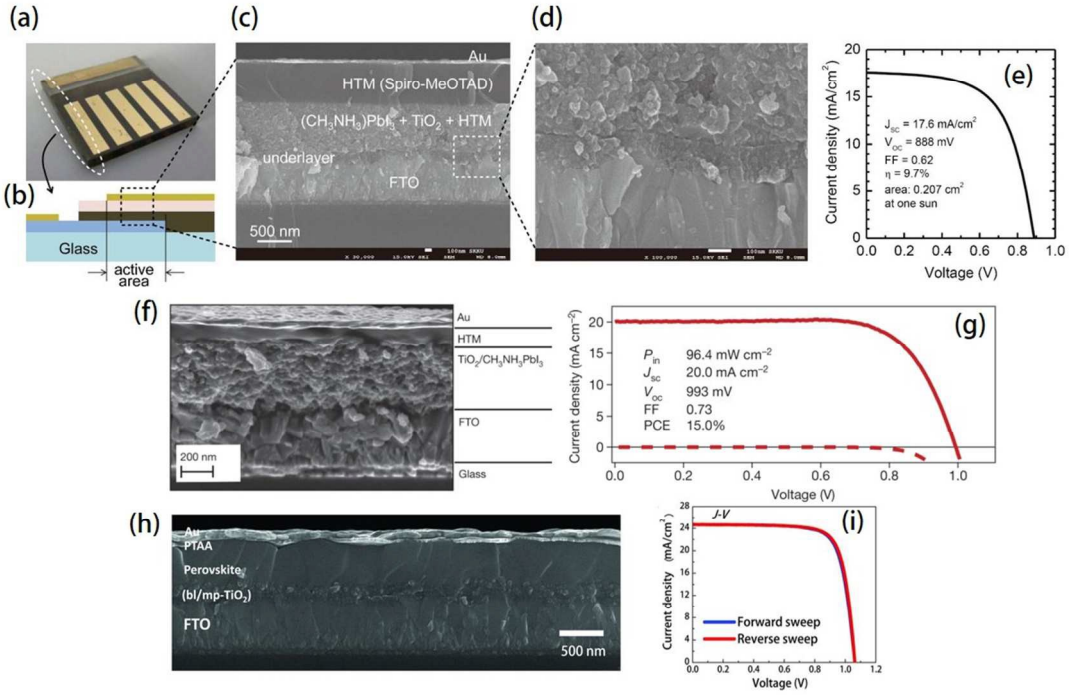

Fig. 2 Device configurations and *J-V* characteristics of mesoscopic PrSCs. (a) Real device of the first solid-state mesoscopic perovskite solar cells. (b) Schematic image of the device cross-section. (c) SEM image of the device cross-section. (d) Magnified cross-sectional SEM image of FTO/underlayer/active layer region. (e) *J-V* characteristic of the device at one sun condition. Reproduced from ref. 1 with permission from Nature Publishing Group. (f) Cross-sectional SEM image of another mesoscopic perovskite solar cells. (g) *J-V* characteristics of the device under a simulated AM1.5G solar irradiation (solid line) and in the dark (dashed line) (reproduced from ref. 3 with permission from Nature Publishing Group). (h) Cross-sectional FESEM image of the device with PCE over 20 %. (i) *J-V* characteristic of the device measured in reverse and forward direction under standard AM 1.5G illumination. Reproduced from ref. 4 with permission from Science (AAAS).

method in which PbI_2 was first deposited on mesoporous metal oxide and transformed into perovskite by exposing methylammonium iodide (MAI).[3] With this method, the devices had greatly increased reproducibility and PCE ≈ 15 % (Fig. 2f, g). Seok *et al*. (2014) achieved PCE = 16.2 % by depositing a uniform and dense perovskite layer by using a mixed solvent of γ-butyrolactone and dimethylsulphoxide (DMSO), then drop-casting toluene.[67] Very recently, Seok *et al*. (2015) achieved a record PCE > 20 % by exploiting intramolecular exchange process between formamidinium iodide (FAI) and DMSO molecules intercalated in PbI_2 (Fig. 2h, i).[4] This remarkably rapid progress in development of PrSCs and several advantages such as thinness, light weight, and inexpensive processability are making PrSCs appropriate for various solar cell applications.

Many electronic devices including PrSCs are being developed toward flexible configuration for future electronics. However, mesoscopic PrSCs cannot easily be made flexible because generally the mesoscopic structure should be sintered at T > 450 °C to function as an EEL in a device,[1–4] but most available flexible substrates (e.g., PET, PEN) have a glass transition temperature that is lower than the sintering temperature, so the polymer substrates deform under high sintering temperature. Therefore, to establish flexible PrSCs, a new device structure that can be fabricated at low T is required.

A PHJ PrSCs that does not use mesoscopic structure is a practical option for flexible PrSCs owing to low-T processability. PHJ PrSCs are divided into two groups according to the layer stacking sequence: i.e., the conventional n-i-p structure in which EEL is deposited on bottom cathode first, HEL is underneath the top anode layer, and the perovskite is sandwiched between EEL and HEL; and the p-i-n structure, which is the inverse of the n-i-p type.

The n-i-p configuration of PHJ devices was introduced in 2013 as a modification of meso-superstructured (MSSC) PrSCs that incorporated mesoporous insulating scaffold of Al_2O_3 on a compact TiO_2 layer.[68] The device had PCE = 4.9 % without mesostructure which is PHJ type; the authors described that $MAPbI_{3-x}Cl_x$ perovskite absorber can fulfil both light absorption and efficient charge transport with minimal recombination in the film. Based on this result, they questioned whether mesostructure is essential in PrSCs. Although the device included a high-T (> 500 °C) processed compact TiO_2 layer, many researchers then sought to develop n-i-p type PHJ PrSCs that could be fabricated using low-T processing.[19,69–82]

The p-i-n type PHJ PrSCs was first developed by Guo *et al*. in 2013.[83] The researchers noticed that the concept of donor/acceptor could be applicable to the device and introduced the structure after referring to a previous work by Etgar *et al*., who reported that $MAPbI_3$ perovskite acts as both light absorber and hole conductor.[84] The first p-i-n PHJ PrSCs

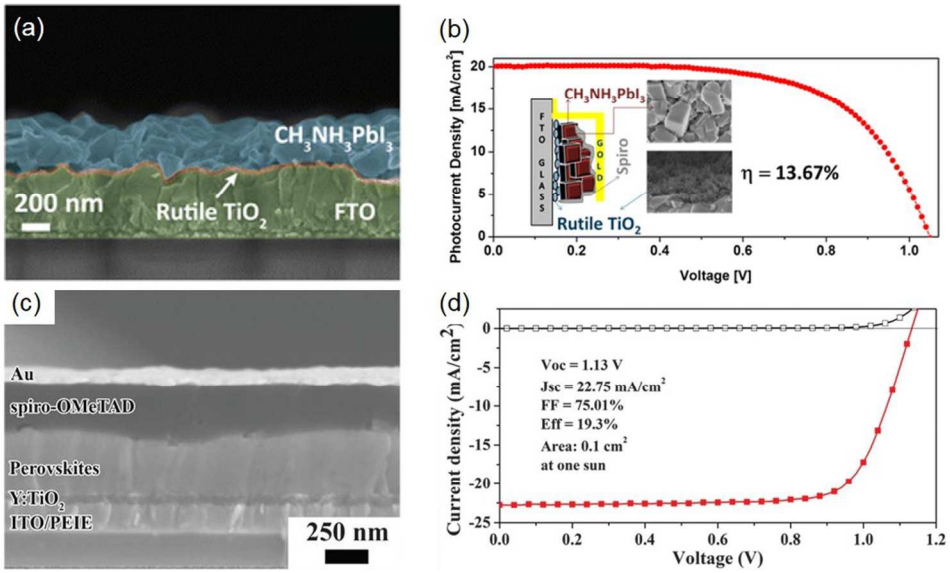

Fig. 3 (a) Cross-sectional SEM image of perovskite film deposited on the nanocrystalline TiO_2 film. (b) *J-V* curves of the n-i-p PHJ PrSC device that used rutile TiO_2. Inset shows schematic image of the device and SEM images of perovskite and rutile TiO_2 layer. Reproduced from ref. 78 with permission from the American Chemical Society). (c) Cross-sectional SEM image of the n-i-p PHJ PrSC device. (d) *J-V* curves of the device. Reproduced from ref. 19 with permission from Science (AAAS).

employed poly(3,4-ethylenedioxythiophene) polystyrene sulfonate (PEDOT:PSS) as a p-type layer for hole extraction, and fullerene-based molecules as an acceptor (n-type) that were deposited on the perovskite (donor) layer. In addition to PEDOT:PSS, various kinds of efficient p-type layers such as NiO_x,[85] CuSCN,[86] graphene oxide (GO)[87] and reduced graphene oxide (rGO)[88] for p-i-n type PHJ PrSCs have been reported. Most p-i-n type devices can be fabricated at T < 150 °C, so this configuration is regarded as the most suitable for flexible devices.

3.2. Progress in low-temperature processed PHJ PrSCs

In this section, we present some examples and progress of solution processed n-i-p and p-i-n type PHJ PrSCs, and vacuum processed PHJ devices.

Solution processed n-i-p (normal) structure. After n-i-p type PHJ PrSCs were shown to be operational, many researchers tried to develop and improve the PCE of the devices. However, most studies on this type of PrSC have described use of a TiO_2 compact layer processed at T > 450 °C, which is not compatible with fabrication of flexible devices.[2,89–104] Therefore, studies on low-T processable EEL have been required.

Grätzel *et al*. improved the suitability of a TiO_2 layer on FTO for electron extraction by immersing the substrate in $TiCl_4$ solution at T = 70 °C;[78] the resultant TiO_2 was a rutile nanoparticle that could form an intimate nanocrystalline junction with a perovskite layer (Fig. 3a). A device with FTO/TiO_2/$MAPbI_3$/Spiro-OMeTAD/Au structure achieved PCE = 13.7 % (Fig. 3b). Boyen *et al*. used TiO_2 layer as an ETL based on titanium isopropoxide processed at low T = 135 °C.[70] The device had ITO/TiO_2/$MAPbI_{3-x}Cl_x$/P3HT/Ag structure and PCE = 13.6 %; the authors stated that the chemical composition and condition of thermal treatment on the TiO_2 film have critical effects on the device performance. Yang *et al*. achieved PCE up to 19.3 % (average 16.6 %) which is so far the highest value in an n-i-p type PHJ PrSCs (Fig. 3c, d).[19] The authors introduced an enhanced reconstruction process for perovskite film by annealing as-deposited film in humidity-controlled air. For efficient electron transport, they chose poly-(ethyleneimine ethoxylated) (PEIE) processed at 100 °C and Yttrium-doped TiO_2 processed at 150 °C. By taking transient photovoltage and photocurrent measurements, they found that extended electron carrier lifetime, reduced trap densities in perovskite film and faster photocurrent decay of the device using modified TiO_2 contributed superior device performance. In addition to TiO_2-based EEL, researchers are developing other low-T processable EELs such as ZnO nanoparticles, CdSe nanocrystals, SnO_2, WO_x, and phenyl-C_{61}-butyric acid methyl ester ($PC_{61}BM$).[67,69,71,72,73,75,77]

Solution processed p-i-n (inverted) structure. The first reported p-i-n type PHJ PrSCs (Section 3.1) achieved PCE = 3.9 % with ITO/PEDOT:PSS/$MAPbI_3$/PCBM/BCP/Al structure (Fig. 4a, b).[83] Although the PCE was much lower compared to mesoscopic PrSCs at that time, this work had significant meaning in developing a new design for PrSCs that could be processed at T < 150 °C. Subsequently, Snaith *et al*. demonstrated devices with FTO/PEDOT:PSS/$MAPbI_{3-x}Cl_x$/PCBM/TiO_x/Al structure, which achieved PCE = 9.8 %,[105] and Yang *et al*. demonstrated a device with ITO/PEDOT:PSS/$MAPbI_{3-x}Cl_x$/PCBM/Al that achieved PCE = 11.5 %.[106]

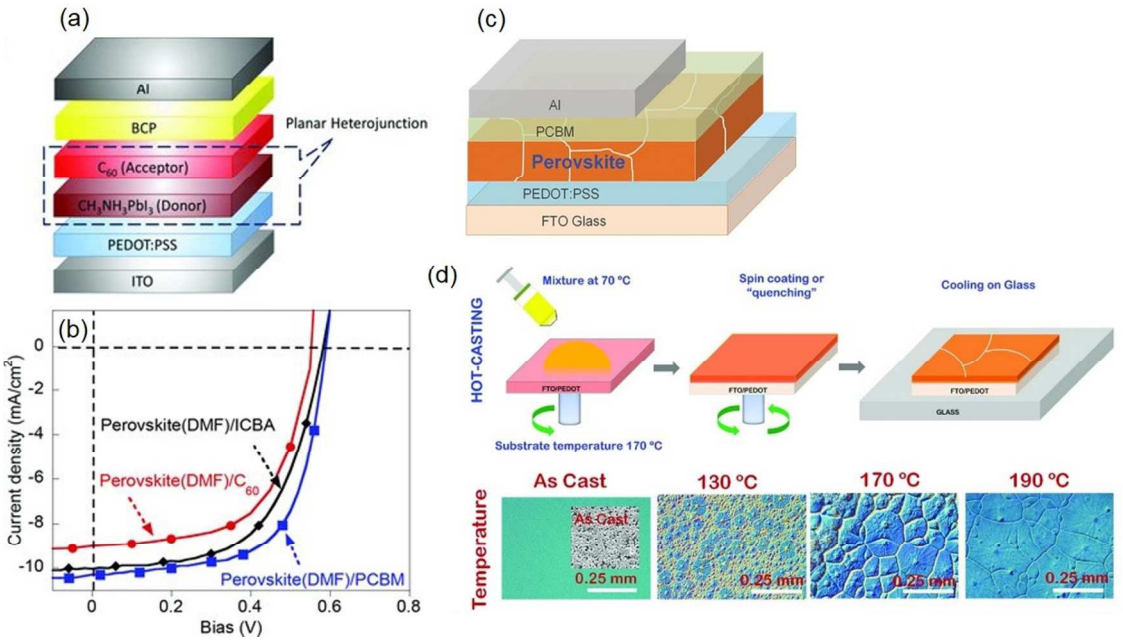

Fig. 4 (a) Device structure of the first p-i-n PHJ PrSCs. (b) *J-V* characteristics of the devices with different acceptor materials. (Reproduced from ref. 83 with permission from Wiley-VCH) (c) Device structure of p-i-n PHJ PrSCs. (d) Processing scheme for formation of perovskite film by hot-casting method and optical microscopic images illustrating grain formation with various conditions. (Reproduced from ref. 46 with permission from Science (AAAS))

Based on these reports of inverted PHJ PrSCs with reasonably high PCEs, many groups have been working on this type of PrSC and have reported increasing PCE. Huang *et al.* used interdiffusion method which is stacking layers of PbI_2 and MAI in sequence by spin-coating.[21] $MAPbI_3$ layer obtained by the method uniformly formed without pin-holes. Controlling the thickness of the perovskite layer, the concentration of MAI solution, and the duration of heating treatment on perovskite yielded a device that had PCE = 15.3 %.

Some research has focused on increasing the grain size and crystallinity of perovskite light absorbers. One method is solvent-annealing method in which $MAPbI_3$ film is exposed to dimethylformamide (DMF) during thermal-annealing.[25] The grain size of solvent-annealed perovskite increased to 1 μm, which was even larger than only thermal-annealed perovskite grain (~ 260 nm). The lower density of grain boundaries in solvent-annealed perovskite film led to the lower density of traps and increased diffusion length of charge carriers. As a result, the device achieved high PCE = 15.6 %. Mohite *et al.* introduced a solution-based hot-casting technique to deposit $MAPbI_{3-x}Cl_x$.[46] The technique uses a hot (70 °C) mixture of PbI_2 and MACl solution, and the solution is cast onto a hot (180 °C) substrate. This method yields millimetre-scale crystalline grains of $MAPbI_{3-x}Cl_x$. The film had reduced bulk defects and improved charge carrier mobility of perovskite so that a device with the perovskite showed very high PCE approaching 18 % with ITO/PEDOT:PSS/$MAPbI_{3-x}Cl_x$/PCBM/Al structure (Fig. 4c, d).

In addition to the explained examples above, numerous other low-*T* and solution-processed PHJ PrSCs have been reported. We give summaries of them including their device structures and photovoltaic parameters (Table 1 for n-i-p PHJ PrSCs and Table 2 for p-i-n PHJ PrSCs). Most research on solution-processed PHJ PrSCs has considered various approaches to engineering of the perovskite layer (e.g., thermal annealing,[24,28,30,70,74,107] solvent-assisted process,[25,29,43,71,108,109] additive treatment[20,23,26,33,34,38,44,72,110] and variation of component materials[22,28,31,36,42,111,112]). Several other studies have considered interfacial layers of PHJ PrSCs.

Vacuum-processed PHJ PrSCs. Exposure to moisture can strongly affect the material properties of perovskite light absorbers.[113–116] Moreover, fabrication of reproducible perovskite films by solution processing is a difficult task due to its high reaction rates of forming perovskites. In this regard, the vacuum evaporation process is attractive based on its advantages in fabrication of PrSCs, including guaranteed material purity, ease of controlling experimental parameters (e.g., deposition rate, thickness and stoichiometry) and high reproducibility of a device.

Development of vacuum-processed PrSCs was initiated in response to scepticism that mesostructure is necessary in PrSCs.[117] The vacuum-processed PrSCs had FTO/compact TiO_2/$MAPbI_{3-x}Cl_x$/Spiro-OMeTAD/Ag structure (n-i-p) without a mesoscopic layer. MAI and $PbCl_2$ were simultaneously deposited from separate sources under vacuum for formation of perovskite film, whereas each interfacial layer was deposited by spin-coating. Compared to solution-processed perovskite film, a thermally-deposited perovskite layer showed superior uniformity. Because of this uniformity, the device

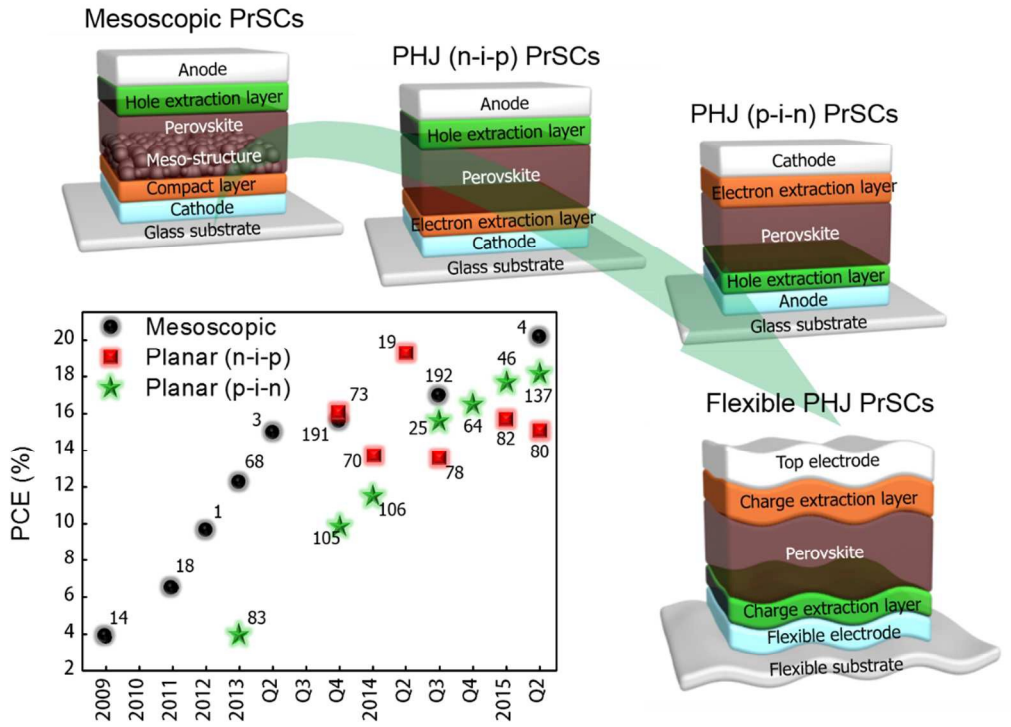

Fig. 5 The green arrow represents improvement in device architecture of PrSCs and the desirable direction of development of PrSCs we suggest. The graph shows progress in PCEs of mesoscopic PrSCs and low-*T* processed PHJ (n-i-p and p-i-n) PrSCs.

showed higher PCE = 15.4 % than did the solution-processed device (8.6 %). However, because the device contained compact TiO_2 layer processed at high *T* (500 °C), it lost compatibility with flexible PrSCs. Bolink *et al*. reported development of p-i-n type PHJ PrSCs with ITO/PEDOT:PSS/PolyTPD/$MAPbI_3$/PCBM/Au structure (PCE ~ 12 %).[118] The perovskite layer was formed by simultaneous deposition of MAI and PbI_2 using separate crucibles under vacuum, and interfacial layers were deposited by a low-*T* solution process. Hence, the device has a potential to be a flexible PrSCs.

Leo *et al*. showed p-i-n type PHJ PrSCs fabricated using a full vacuum process.[119] Fully vacuum-processed devices have the merit of not being exposed to air or solvent, so the devices can have longer lifetime than devices fabricated with some exposure to air or solvent.[120] In their work, a series of HELs in a family of triarylamine derivatives were used in devices. The authors presented the influence of energy level offsets between HELs and $MAPbI_{3-x}Cl_x$ on device performance. Another fully vacuum-processed p-i-n type PHJ PrSCs with ITO/MoO_3/NPB/$MAPbI_3$/C_{60}/BCP/Al structure was reported by Kim *et al*.[121] The device showed high PCE = 13.7 %, which was attributed to efficient hole extraction of MoO_3/NPB, and energy level alignment between HOMO level of NPB and valence band maximum (VBM) level of perovskite.

4. Roles of interfacial layers in planar heterojunction perovskite solar cells

Although fewer studies have considered interfacial layer engineering than perovskite layer engineering for optimum morphology, this difference does not mean that interfacial layer engineering is trivial. To increase the PCE of photovoltaic devices, interfacial layers should be understood in depth and properly used in PHJ PrSCs.[122,123] In this section, we review studies of the interfacial layer engineering of PHJ PrSCs, and give an insight into its roles. Among several functions of interfacial layers in PHJ PrSCs, we will discuss its contributions to energy level alignment, electrical conductivity, trap passivation and the effect on device long-term stability in special.

4.1. Energy-level tailoring

Energy-level tailoring is one of the most effective ways to directly increase device performance. Appropriate energy-level tailoring can increase V_{oc} and facilitate charge transfer and extraction, which contribute to increasing J_{sc} and FF.[124] Especially, because V_{oc} of PrSCs is determined by quasi-Fermi level difference between HEL and EEL, reducing the energy level offset between VBM of perovskite and IE of HEL, and between conduction band minimum (CBM) of perovskite and EA of EEL is crucial to increase the quasi-Fermi level

difference.[125–130] Here, we present examples of energy-level tailoring of HELs and EELs.

Hole extraction layers. Interfacial layers in PHJ PrSCs should be carefully selected considering the energy level of intimate layers. However, the most widely-used perovskite light absorbers $MAPbI_3$, $MAPb_{3-x}Cl_x$, $MAPbBr_3$, and $FAPbI_3$ have relatively high IEs (5.4, 5.4, 5.9 and 5.4 eV, respectively) compared to commonly-used HELs such as PEDOT:PSS, spiro-OMeTAD, and Poly(triarylamine) (PTAA) (4.9 ~ 5.2 eV). The

Device architecture	V_{oc} (V)	J_{sc} (mA/cm^2)	FF (%)	PCE (%)	Remarks	Ref.
ITO/ZnO NP/MAPbI$_3$/P3HT[i]/Ag	0.94	17	62	11.8	P[a]: Control of morphology (thickness)	69
ITO/TiO$_2$/MAPbI$_{3-x}$Cl$_x$/P3HT/Ag	0.936	21.0	69.1	13.6	P: Control of morphology (TA[d] time)	70
ITO/SnO$_2$/MAPbI$_3$/spiro-OMeTAD[n]/Ag	1.08	19.5	61.6	13.0	P: Control of morphology (SA[e] time)	71
FTO/TiO$_2$/MAPbI$_{3-x}$Cl$_x$/spiro-OMeTAD/Au	0.94	19.53	70.35	13.2	P: Additive (poly(ethylene glycol))	72
ITO/ZnO nanoparticles/MAPbI$_3$/spiro-OMeTAD/Ag	1.03	20.4	74.9	15.7	E[b]: Control of thickness	73
ITO/CdSe nanocrystal/MAPbI$_3$/spiro-OMeTAD/Ag	0.99	17.4	67.9	11.7	E: Control of thickness and TA temperature	74
FTO/PEI[j]/PC$_{61}$BM/MAPbI$_3$/PTAA[k]/Au	0.98	21.8	72	15.3	E: Control of concentration	75
ITO/Zr-TiO$_2$/MAPbI$_{3-x}$Cl$_x$/spiro-OMeTAD/Au	1.021	20.3	76.6	15.7	E: Additive (ZrAc$_4$)	76
ITO/PEIE[l]/Y:TiO2/MAPbI$_{3-x}$Cl$_x$/spiro-OMeTAD/Au	1.13	22.75	75.01	19.3	E: Doping (Yttrium)	19
ITO/ZnO/C$_3$-SAM[m]/MAPbI$_3$/spiro-OMeTAD/MoO$_3$/Ag	1.07	22.51	65	15.67	E: SAM[f] deposition (3-aminopropanoic acid)	82
FTO/TiO$_2$/MAPbI$_3$/spiro-OMeTAD/Au	1.05	19.8	64	13.7	E: Use of rutile TiO$_2$	78
FTO/WO$_x$/MAPbI$_{3-x}$Cl$_x$/spiro-OMeTAD/Ag	0.71	21.77	58	8.99	E: Use of WO$_x$	79
ITO/TiO$_x$/PC$_{61}$BM/WS-C$_{60}$/MAPbI$_3$/P3HT/MoO$_x$/Al	0.95	27.4	56.3	14.6	E: Comparison of TiO$_2$, TiO$_2$/PC$_{61}$BM and TiO$_2$/PC$_{61}$BM/WS-C$_{60}$[g]	131
FTO/TiO$_2$/MAPbI$_3$/spiro-OMeTAD/spiro-OMeTAD:MWNTs/Au	-	-	-	15.1	H[c]: Additive (MWNTs[h]) and use of hierarchical structure	80
ITO/TiO$_2$/MAPbI$_{3-x}$Cl$_x$/DOR3T-TBDT/MoO$_3$/Ag	0.97	20.7	74	14.9	H: Dopant-free	81
FTO/ZnO nanoparticles/MAPbI$_3$/Carbon	0.77	18.56	56	8.07	Use of carbon electrode	77

[a] P: perovskite layer engineering. [b] E: EEL engineering. [c] H: HEL engineering. [d] TA: thermal annealing. [e] SA: solvent annealing. [f] SAM: self-assembling monolayer. [g] WS-C$_{60}$: water-soluble fullerene derivative. [h] MWNT: multi-walled carbon nanotube. [i] P3HT: poly(3-hexylthiophene-2,5-diyl). [j] PEI: polyethyleneimine. [k] PTAA: Poly(triarylamine). [l] PEIE: poly-(ethyleneimine ethoxylated). [m] C3-SAM: 3-aminopropanioc acid. [n] spiro-OMeTAD: 2,20,7,70-tetrakis(N,N0-di-p-methoxyphenylamine)-9,90-spirobifluorene.

Table 1 Summary of information of solution processed n-i-p PHJ PrSCs at low-*T*.

Table 2 Summary of information of solution processed p-i-n PHJ PrSCs at low-*T*.

Device architecture	V_{oc} (V)	J_{sc} (mA/cm^2)	FF (%)	PCE (%)	Remarks	Ref.
FTO/PEDOT:PSS/MAPbI$_{3-x}$Cl$_x$/PC$_{61}$BM/TiO$_x$/Al	0.94	15.8	66	9.8	Comparison between p-i-n and MSSC[d] devices	105
ITO/PEDOT:PSS/MAPbI$_{3-x}$Cl$_x$/PC$_{61}$BM/Al	0.87	18.5	72	11.5	Demonstration of low-*T* processability	106
ITO/PEDOT:PSS/MAPb$_{0.85}$Sn$_{0.15}$I$_{3-x}$Cl$_x$/Bis-C$_{60}$ /PC$_{61}$BM/Ag	0.76	19.1	66	10.1	P[a]: Substitution of Sn for Pb	111
ITO/PEDOT:PSS/MAPbI$_{3-x}$Cl$_x$/PC$_{61}$BM/Bis-C$_{60}$/Ag	0.92	17.5	73	11.8	P: Additive (1,8-diiodooctane)	20
ITO/PEDOT:PSS/MAPbI$_3$/PC$_{61}$BM/C$_{60}$/BCP/Al	0.96	21.0	76	15.6	P: Control of morphology (thickness and SA[e])	25
ITO/PEDOT:PSS/MAPbI$_{3-x}$Cl$_x$/PC$_{61}$BM/PFN/Al	1.05	20.3	80.2	17.1	P: Control of morphology (TA[f] environment)	107
ITO/PEDOT:PSS/MAPbI$_{3-x}$Cl$_x$/PC$_{61}$BM/C$_{60}$/Ag	0.91	18.3	70	11.65	P: Control of morphology (precursor ratio)	36
ITO/PEDOT:PSS/MAPbI$_{3-x}$Cl$_x$/PC$_{61}$BM/Ca/Al	0.92	16.8	72	11.1	P: Control of thickness and morphology (substrate heating), and use of spray coating method	132
ITO/PEDOT:PSS/MAPbI$_3$/PC$_{61}$BM/C$_{60}$/BCP/Al	0.99	19.6	79.3	15.4	P: Control of thickness and concentration of MAI	21
ITO/PEDOT:PSS/MAPbI$_3$/IC$_{60}$BA/C$_{60}$/BCP/Al	0.97	15.7	80.1	12.2	P: Control of morphology (precursor ratio) and thickness, E[b]: Comparison of PC$_{61}$BM[u]/C$_{60}$, IC$_{60}$BA[v]/C$_{60}$ and C$_{60}$	22
ITO/PEDOT:PSS/MAPbI$_3$/PC$_{61}$BM/Al	0.91	10.8	76	7.4	P: Control of thickness	133
ITO/PEDOT:PSS/MAPbI$_{3-x}$Cl$_x$/PC$_{61}$BM/Bis-C$_{60}$/Ag	0.94	18.47	75	13.09	P: Additive (1,4-diiodobutane)	23
ITO/PEDOT:PSS/MAPbI$_3$/PC$_{71}$BM/Ca/Al	1.05	19.98	78	16.31	P: Control of concentration of MAI, E: Comparison between PC$_{61}$BM and PC$_{71}$BM, and control of SA time	108
ITO/PEDOT:PSS/MAPbI$_3$/PC$_{61}$BM/C$_{60}$/BCP/Al	~0.9	19.0	78	13.4	P: Control of morphology (TA time)	24
ITO/PEDOT:PSS/MAPbI$_3$/PC$_{71}$BM/Ag	0.87	18.66	75	12.22	P: Control of morphology (precursor solvent), E: Comparison between PC$_{61}$BM and PC$_{71}$BM	134
ITO/PEDOT:PSS/MAPbI$_{3-x}$Cl$_x$/PC$_{61}$BM/Al	0.91	17.27	75	11.80	P: Control of morphology (solvent evaporation rate)	37
ITO/PEDOT:PSS/Cs$_{0.1}$MA$_{0.9}$PbI$_3$/PC$_{61}$BM/Al	1.05	10.10	73	7.68	P: Substitution of Cs for MA	112
ITO/PEDOT:PSS/MAPbI$_3$/PC$_{61}$BM/Al	0.88	14.08	80.11	9.93	P: Additive (NH$_4$Cl)	26

ITO/PEDOT:PSS/$MAPbI_3$/$PC_{61}BM$/Al	0.92	8.74	76	6.16	P: Control of morphology (precursor solvent)	27
ITO/PEDOT:PSS/$MAPbI_{3-x}Cl_x$/$PC_{61}BM$/Al	0.86	14.3	60.9	7.5	P: Control of morphology (precursor ratio, TA temperature and time)	28
ITO/PEDOT:PSS/$MAPbI_3$/$PC_{61}BM$/C_{60}/BCP/Al	0.96	21.0	76	15.6	E: Trap passivation (TA time)	50
ITO/PEDOT:PSS/$MAPbI_3$/$PC_{61}BM$/Bis-C_{60}/Ag	0.91	19.3	80	14.1	P: Control of morphology (solvent washing)	29
ITO/PEDOT:PSS/$MAPbI_3$/$PC_{61}BM$/PFN-Br/Ag	1.03	18.36	78	14.75	P: Control of morphology (vacuum-assisted TA)	30
ITO/PEDOT:PSS/$MAPbI_3$/$PC_{61}BM$/Bis-C_{60}/Ag	0.91	18.38	73	12.21	P: Use of blade-coating method	135
ITO/PEDOT:PSS/$MAPbI_xCl_{3-x}$/$PC_{61}BM$/Bis-C_{60}/Ag	0.89	16.0	74	10.5	P: Substitution of Br for I_xCl_{3-x}	31
ITO/PEDOT:PSS/$MAPbI_3$/$PC_{61}BM$/C_{60}/BCP/Al	0.93	17.3	63	10.2	P: Use of spray-coating method	136
ITO/PEDOT:PSS/$MAPbI_{3-x}Cl_x$/$PC_{61}BM$/Al	0.854	16.7	63.4	8.97	P: Additive (1-chloronaphthalene)	33
ITO/PEDOT:PSS/$MAPbI_3$/$PC_{61}BM$/Ca/Al	0.91	13.11	78.11	9.32	P: Additive (NH_4Cl)	38
ITO/PEDOT:PSS/$MAPbI_3$/$PC_{61}BM$/Ca/Au	1.1	20.9	79	18.2	Comparison between p-i-n and n-i-p structure	137
ITO/PEDOT:PSS/$MAPbI_{3-x}Cl_x$/$PC_{61}BM$/ZnO/Al	1.027	22.0	74.2	16.8	P: Control of morphology (growth rate)	39
ITO/PEDOT:PSS/$MAPbI_{3-x}Cl_x$/$PC_{61}BM$/Al	0.86	16.8	70.4	10.9	P: Additive (ethylammonium iodide)	34
ITO/PEDOT:PSS/$MAPbI_{3-x}Cl_x$/$PC_{61}BM$/Ag	0.91	17.76	73	11.82	P: Comparison between ($MAPbI_{3-x}Cl_x$ and $MAPbI_3$)	138
ITO/PEDOT:PSS/$MAPbI_3$/$PC_{61}BM$/C_{60}/BCP/Al	0.90	20.00	75.1	13.60	P: Control of morphology (vapour atmosphere)	40
ITO/PEDOT:PSS/$MAPbI_3$/$PC_{61}BM$/C_{60}/BCP/Al	0.91	21.06	60.84	11.66	P: Control of morphology (liquid droplet assisted)	139
ITO/PEDOT:PSS/$MAPbI_3$/$PC_{61}BM$/BCP/Al	0.83	19.86	59	9.75	P: Control of morphology (solvent-assisted deposition)	109
ITO/PEDOT:PSS/$MAPbI_{3-x}Cl_x$/$PC_{61}BM$/Al	0.95	19.79	63.2	11.88	P: Control of morphology (thickness)	41
ITO/PEDOT:PSS/$MAPbI_3$/$PC_{61}BM$/Al	0.99	19.99	63	13.49	P: Control of morphology (precursor ratio, thickness)	42
ITO/PEDOT:PSS/$MAPbI_{3-x}Cl_x$/$PC_{61}BM$/C_{60}/Al	0.934	19.48	72.07	13.11	P: Control of morphology (IPA treatment)	43
ITO/PEDOT:PSS/$MAPbI_{3-x}Cl_x$/$PC_{61}BM$/LiF/Al	0.979	18.79	68.8	12.73	P: Additive (1,8-diiodooctane)	44
ITO/PEDOT:PSS/$MAPbI_3$/$PC_{61}BM$/Al	1.04	8.85	65.2	6.16	P: Additive (Poly(2-ethyl-2-oxazoline))	110
FTO/PEDOT:PSS/$MAPbI_{3-x}Cl_x$/$PC_{61}BM$/Al	0.94	22.4	83	17.5	P: Control of morphology (hot-casting method)	46
ITO/PEDOT:PSS/$MAPbI_3$/$PC_{61}BM$/Al	0.86	17.31	77.2	11.45	P: Control of morphology (precursor solvent)	45
ITO/PEDOT:PSS/$MAPbI_{3-x}Cl_x$/$PC_{61}BM$/Al	0.92	15.4	68.2	9.6	H[c]: Additive (Ag nanoplates)	140
ITO/SOHEL[t]/$MAPbI_3$/$PC_{61}BM$/Al	0.982	16.7	70.5	11.7	H: Additive (perfluorinated ionomer) into PEDOT:PSS, tuning WF	141
ITO/polythiophene/$MAPbI_3$/C_{60}/BCP/Ag	1.03	16.2	70.7	11.8	H: Control of thickness	142
ITO/Poly-TPD/$MAPbI_3$/$PC_{61}BM$/C_{60}/BCP/Ag	1.1	22.0	69.7	15.3	H: Use of Poly-TPD	143
ITO/MoO_3/PEDOT:PSS/$MAPbI_3$/C_{60}/Bphen/Ag	0.96	20.06	67	12.78	H: Insertion of MoO_3 and Control of solution MoO_3 concentration	144
ITO/rGO/$MAPbI_3$/$PC_{61}BM$/BCP/Ag	0.95	14.81	71.13	10.80	H: Use of rGO[g]	88
ITO/PEDOT:PSS-AgNPs/$MAPbI_{3-x}Cl_x$/$PC_{61}BM$/Bphen/Ag	0.93	21.51	79	15.75	H: Additive (Ag nanoparticles), E: Control of concentration of Bphen solution	145
ITO/GO/$MAPbI_{3-x}Cl_x$/$PC_{61}BM$/ZnO/Al	1.00	17.46	71	12.4	H: Use of GO[h] and control of its concentration	87
ITO/PEDOT:PSS/$MAPbI_3$/$PC_{61}BM$/BCP/Al	0.6	10.32	63	3.9	E: Comparison of C_{60}, $PC_{61}BM$ and $IC_{60}BA$	83
ITO/PEDOT:PSS/$MAPbI_{3-x}Cl_x$/$PC_{61}BM$/PEIE/Ag	0.899	17.32	77.1	12.01	E: Comparison of methanol, PEIE[i] and P3TMAHT[j]	146
ITO/PEDOT:PSS/$MAPbI_3$/$PC_{61}BM$/LiF/Al	0.846	20.2	76.7	13.1	E: Insertion of LiF, Control of $PC_{61}BM$ thickness	147
ITO/PEDOT:PSS/$MAPbI_{3-x}Cl_x$/$PC_{61}BM$/PN_4N/Ag	1.00	20.61	72.5	15.0	E: Comparison of PN_4N[k], IPA[l], PFN[m] and methanol	148
ITO/PEDOT:PSS/$MAPbI_{3-x}Cl_x$/$PC_{61}BM$/ZnO/Al	0.83	14.65	70	9.47	E: Comparison of $PC_{61}BM$, N2200[n], PNVT-8[o] and PNDI2OD-TT	149
ITO/PEDOT:PSS/$MAPbI_{3-x}Cl_x$/$PC_{61}BM$/DMAPA-C_{60}/Ag	0.97	17.9	77	13.4	E: Insertion of DMAPA-C_{60}	150
ITO/PEDOT:PSS/$MAPbI_3$/C_{60}/Bis-C_{60}/Ag	0.92	21.07	80	15.44	E: Comparison of $IC_{60}BA$, $PC_{61}BM$ and C_{60}	151
ITO/PEDOT:PSS/$MAPbI_3$/$PC_{61}BM$/$PC_{61}BM$/Ag	0.99	18.11	68	12.2	E: Use of double $PC_{61}BM$ layer	152
ITO/PEDOT:PSS/$MAPbI_{3-x}Cl_x$/$PC_{61}BM$/PDINO/Ag	0.95	18.8	78.5	14.0	E: Comparison between ZnO and PDINO[p]	153
ITO/PEDOT:PSS/$MAPbI_{3-x}Cl_x$/$PC_{61}BM$/PCBC/Al	0.98	22.08	69.7	15.08	E: Comparison between LiF and PCBC[q]	154
ITO/PEDOT:PSS/$MAPbI_{3-x}Cl_x$/$PC_{61}BM$:graphdiyne /C_{60}/Al	0.969	23.4	65.4	14.8	E: Doping (graphdiyne)	155
ITO/PEDOT:PSS/$MAPbI_{3-x}Cl_x$/$PC_{61}BM$/Rhodamine101 /LiF/Al	1.01	17.72	73	13.2	E: Insertion of Rhodamine 101	156
FTO/PEDOT:PSS/$MAPbI_3$/$PC_{61}BM$/TIPD/Al	0.89	22.57	64.5	12.95	E: Insertion of TIPD[r]	157
ITO/PEDOT:PSS/$MAPbI_{3-x}Cl_x$/$PC_{61}BM$/TPPI/Al	0.90	19.7	73	13.0	E: Insertion of TPPI, P: Additve (TPPI)[s]	158

[a] P: perovskite layer engineering. [b] E: EEL engineering. [c] H: HEL engineering. [d] MSSC: meso-superstructured. [e] SA: solvent annealing. [f] TA: thermal annealing. [g] rGO: reduced graphene oxide. [h] GO: graphene oxide. [i] PEIE: poly-(ethyleneimine ethoxylated). [J] P3TMAHT: poly[3-(6-trimethylammoniumhexyl)thiophene]. [k] PN_4N: amino-functionalized polymer. [l] IPA: isopropanol. [M] PFN: poly [(9,9-bis(3′-(N,N-dimethylamino)propyl)-2,7-fluorene)-alt-2,7-(9,9–dioctylfluorene)]. [n] N2200: poly{[N,N′-bis(2-octyldodecyl)-1,4,5,8-naphthalene diimide-2,6-diyl]-alt-5,5′-(2,2′-bithiophene)}. [O] PNVT-8: poly{[N,N′-bis(alkyl)-1,4,5,8-naphthalene diimide-2,6-diyl-alt-5,5′-di(thiophen-2-yl)-2,2′-(E)-2-(2-(thiophen-2-yl)vinyl)thiophene]}. [p] PDINO: perylene-diimide. [q] PCBC: [6,6]-phenyl-C61-butyric acid (18-crown-6)-2-yl methyl ester. [r] TIPD: titanium (diisopropoxide) bis(2,4-pentanedionate). [S] TPPI: tetraphenylphosphonium iodide. [t] SOHEL: self-organized hole extraction layer. [u] $PC_{61}BM$: [6,6]-Phenyl C_{61} butyric acid methyl ester. [v] $IC_{60}BA$: indene-C_{60} bisadduct.

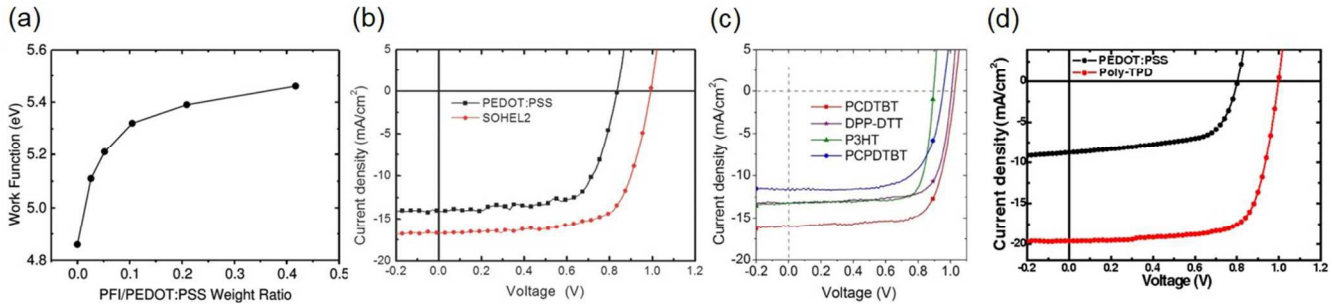

Fig. 6 Energy level tailoring of HELs for PHJ PrSCs (a) Work function change of SOHEL series as a function of the PFI/PEDOT:PSS weight ratio. (b) *J*–*V* characteristics of the PHJ PrSCs with pristine PEDOT:PSS or optimal SOHEL as a HEL. Reproduced from ref. 141 with permission from Wiley-VCH. *J*–*V* characteristics of the PHJ PrSCs with various HELs with difference IEs (c) PCDTBT, DPP-DTT, P3HT and PCPDTBT (Reproduced from ref. 64 with permission from Nature Publishing Group); (d) PEDOT:PSS and Poly-TPD (Reproduced from ref. 143 with permission from Wiley-VCH).

difference between the energy levels of perovskite and the HEL causes loss in built-in potential of a device; this loss can lead to decrease in all photovoltaic parameters such as V_{oc}, J_{sc} and FF. Therefore, to increase PCE of a PHJ PrSCs, energy-level tailoring of an interfacial layer at the junction between perovskite layer and metal contact is essential.

To reduce energy level offset between PEDOT:PSS and $MAPbI_3$ in p-i-n PHJ PrSCs, Lee *et al*. developed a HEL with high work function (WF); this HEL is composed of PEDOT:PSS and a perfluorinated ionomer (PFI) which they called a self-organized hole extraction layer (SOHEL).[141] The WF of this SOHEL could be tuned by adjusting the concentration of PFI in PEDOT:PSS because the surface energy difference between PEDOT:PSS and PFI causes PFI which has high WF to become enriched on the film surface (Fig 6a). This approach is useful to adjust the energy level of a HEL to align with VBM of diverse perovskite materials. A PFI/PEDOT:PSS weight ratio ~ 0.2 (SOHEL2) yielded a HEL with higher WF (5.39 eV) than pristine PEDOT:PSS (4.86 eV). The increased WF was well aligned with the VBM of the $MAPbI_3$. As a result, the device with SOHEL2 achieved PCE = 11.7 % that exceeded that of the device with pristine PEDOT:PSS (PCE = 8.1 %) (Fig. 6 b).

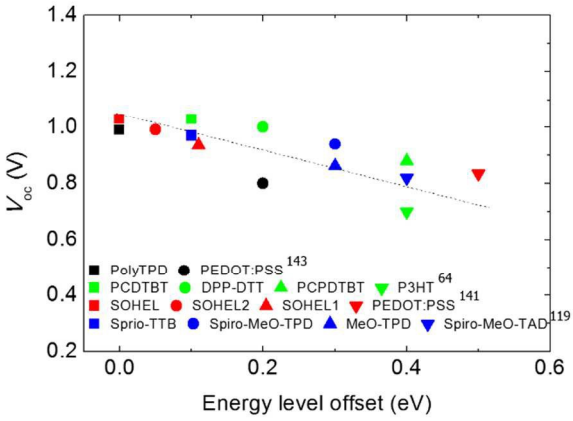

Fig. 7 Change in V_{oc} of PHJ PrSCs as a function of energy level offset between HELs and perovskite.

Burn *et al*. introduced various kinds of *p*-type polymeric organic semiconductors (e.g., DPP-DTT (poly(2,5-(2-di(thien-2-yl)thieno[3,2-b]thiophene))), PCDTBT (poly(N-9′-heptadecanyl-2,7-carbazole-alt-5,5-(4′,7′-di(thien-2-yl)-2′,1′,3′-benzothiadiazole))), P3HT (poly(3-n-hexylthiophene)) and PCPDTBT (poly(2,6-(4,4-bis(2-ethylhexyl)-4H-cyclopenta[2,1-b;3,4-b′]dithiophene)-alt-4′,7′-(2′,1′,3′-benzothiadiazole)))) as a hole interfacial layer in a p-i-n PHJ PrSCs.[64] The polymers modified the WF of ITO/PEDOT:PSS and thereby reduced the potential barrier at the junction between PEDOT:PSS and perovskite, $MAPbI_3$. IEs of the polymers were 5.0 eV for P3HT, 5.0 eV for PCPDTBT, 5.2 eV for DPP-DTT, and 5.3 eV for PCDTBT. When the polymer was introduced onto PEDOT:PSS, the device with polymer of higher IE showed higher V_{oc} in general. The average V_{oc} of devices with PCDTBT interlayer was 1.03 V higher than those of devices with P3HT (0.7 V) (Fig. 6c). The significant increase in V_{oc} arose from reduction in energy level difference between VBM of $MAPbI_3$ and IE of the interfacial polymer layer, thereby increase in quasi-Fermi level difference between EEL and HEL. In a similar way, Poly-TPD can be used to tailor the energy level as a HEL.[118,143,159] Because Poly-TPD has a higher IE (5.4 eV) than does PEDOT:PSS (5.2 eV), the energy offset with $MAPbI_3$ was decreased. Therefore, the device with Poly-TPD showed higher V_{oc} (1.1 V) than that did the device with PEDOT:PSS (0.8 V) (Fig. 6d).

Small-molecule HELs can also be used to tune energy levels. Leo *et al*. explained relation between IE of small-molecule HELs and V_{oc} of fully vacuum-processed p-i-n PHJ PrSCs. For comparison, six HELs with different IEs (Spiro-MeO-TAD (5.0 eV), MeO-TPD (5.1 eV), Spiro-MeO-TPD (5.1 eV), Spiro-TTB (5.3 eV), Sprio-TAD (5.4 eV) and BPAPF (5.6 eV) were chosen from a family of triarylamine derivatives.[119] Devices that used HELs with IEs up to 5.3 eV which is close to VBM of $MAPbI_{x-3}Cl_x$ (5.4 eV) showed gradual increase in V_{oc} of devices from 0.82 V to 0.97 V; the increase in V_{oc} was due to reduction of energy level difference between HEL and perovskite, which increased quasi-Fermi level difference in the devices.

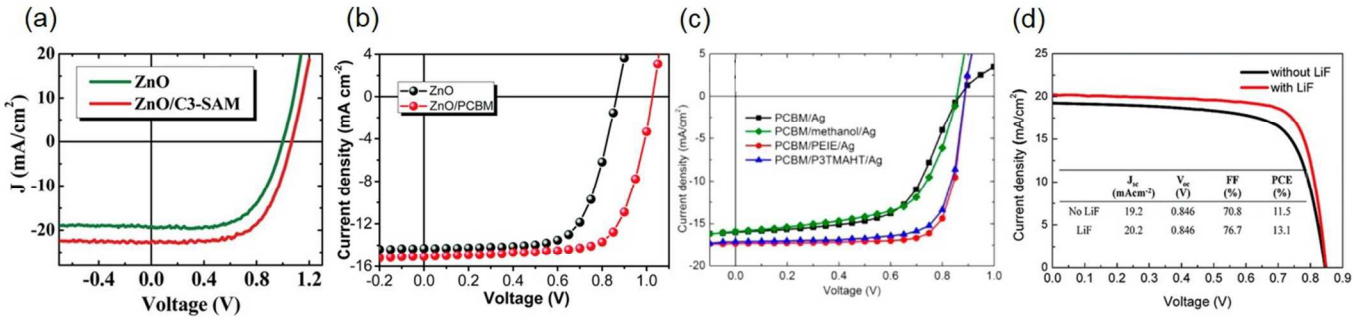

Fig. 8 *J–V* characteristics of the PHJ PrSCs with energy level tailored EELs (a) C3-SAM (Reproduced from ref. 82 with permission from the American Chemical Society) (b) $PC_{61}BM$ (Reproduced from ref. 160 with permission from The Royal Society of Chemistry) (c) PEIE and P3TMAHT (Reproduced from ref. 146 with permission from the American Chemical Society) (d) LiF (Reproduced from ref. 147 with permission from The Royal Society of Chemistry).

Overall changes in V_{oc} of devices described above were linearly proportional to the energy level difference between perovskites and various HELs (Fig. 7). As energy level offset approaches zero, V_{oc} tends to be maximized. This trend strongly indicates that to increase PCE of a device, the HEL must be chosen appropriately, considering its energy level. More specific information of the devices are summarized (Table 3).

Electron extraction layers. Energy level tailoring of the electron extraction side can be explained in a similar manner as in the HEL section. An EEL is required to form good energy-level matching at the junction between cathode and perovskite layer. Otherwise, loss in built-in potential and V_{oc}, and associated decrease in PCE can arise, the commonly-used EELs, TiO_2 and ZnO have CBM around 4.0 ~ 4.2 eV which is quite different from CBM of perovskites: $MAPbI_3$, $MAPb_{3-x}Cl_x$, $MAPbBr_3$, and $FAPbI_3$ generally have CBM in the range of 3.6 ~ 3.9 eV.

Use of self-assembling monolayers (SAM) is an effective way to tailor the energy level of a layer; the effect results from formation of permanent dipole in the SAM. The deposition of 3-aminopropanoic acid SAM (C_3-SAM) onto sol-gel ZnO successfully decreased WF of ZnO from 4.17 to 3.52 eV, and thereby improved its energy level alignment with CBM of $MAPbI_3$ perovskite (3.75 eV).[82] As a result, n-i-p PHJ PrSCs with SAM treatment showed higher V_{oc} (1.07 V) than did the reference device (0.99 V) (Fig. 8a). The energy level of sol-gel ZnO was also tuned by deposition of a thin organic surface modifier, PCBM onto it. The deposition of PCBM changed the electronic structure of the ZnO film into more favourable form.[160] Specifically, use of a ZnO/PCBM EEL decreased the energy level offset with CBM of $MAPbI_3$ and as a result increased the difference in quasi-Fermi levels in a device compared to that in a device with ZnO alone. Therefore, the device with ZnO/PCBM EEL had a higher V_{oc} (1.02 V) than did a device with a ZnO-only EEL (0.78 V) (Fig. 8b). Also, efficient charge transfer and extraction by the favourable energy level alignment increased J_{sc} and FF in the device with ITO/ZnO/PCBM/$MAPbI_3$/PTB7-Th/MoO_3/Ag; as a result it achieved PCE = 12.2 %.

$PC_{61}BM$ is a representative material as EEL in p-i-n PHJ PrSCs because it has excellent electron accepting property.

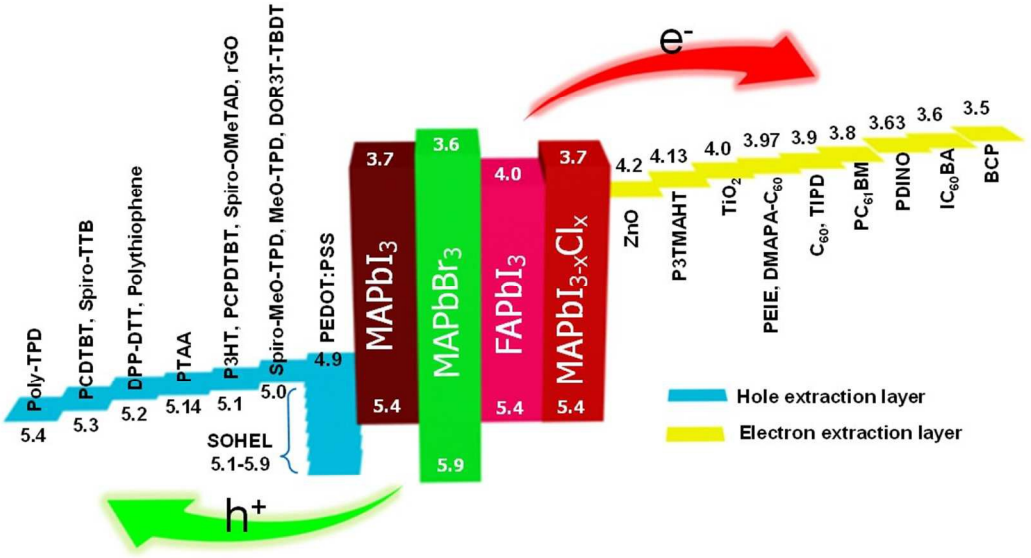

Fig. 9 Energy level diagram of HELs (left) and EELs (right) used in PHJ PrSCs and perovskite light absorbers (middle). The unit for each value is [eV] but omitted. The values of IEs of HELs and EAs of EELs were extracted from the references which are provided in Section 4.1. The energy levels of $MAPbI_3$, $MAPbI_{3-x}Cl_x$ and $MAPbBr_3$ were extracted from ref. 47. The energy level of $FAPbI_3$ was extracted from ref. 196.

HEL	IE of HEL (eV)	Perovskite	VBM of perovskite (eV)	Offset (eV)	V_{oc} (V)	J_{sc} (mA/cm^2)	FF (%)	PCE (%)	Device architecture	Ref
PCDTBT [a]	5.3	$MAPbI_3$	5.4	0.1	1.03	15.9	66	10.9	ITO/PEDOT:PSS/HEL/ $MAPbI_3$/PCBM[l]/LiF/Ag	64
DPP-DTT [b]	5.2			0.2	1.00	13.3	74	9.8		
PCPDTBT [c]	5.0			0.4	0.88	13.0	69	7.8		
P3HT [d]	5.0			0.4	0.7	14.2	78	8.5		
SOHEL [e]	5.39	$MAPbI_3$	5.43	0.04	0.982	16.7	70.5	11.7	ITO/HEL/$MAPbI_3$/ $PC_{61}BM$/Al	141
PEDOT:PSS [f]	4.9			0.53	0.835	14.1	68.5	8.1		
Spiro-TTB [g]	5.3	$MAPbI_{3-x}Cl_x$	5.4	0.1	0.970	14.9	63	9.1	ITO/HEL/$MAPbI_{3-x}Cl_x$/ C_{60}/Ag	119
Sprio-MeO-TPD [h]	5.1			0.3	0.940	15.5	66	9.6		
MeO-TPD [i]	5.1			0.3	0.863	14.5	63	7.8		
Sprio-MeO-TAD [J]	5.0			0.4	0.820	14.1	63	7.2		
Poly-TPD [k]	5.4	$MAPbI_3$	5.4	0	0.99	20.01	69.55	13.78	ITO/HEL/$MAPbI_3$/$PC_{61}BM$/ C_{60}/BCP[m] /Ag	143
PEDOT:PSS	5.2			0.2	0.80	9.41	61.80	4.63		

*We surveyed relevant articles that compared HELs in PHJ PrSCs and exhibited energy levels of HELs, perovskites and corresponding device performance.
[a] PCDTBT: poly(N-9′-heptadecanyl-2,7-carbazole-alt-5,5-(4′,7′-di(thien-2-yl)-2′,1′,3′-benzothiadiazole. [b] DPP-DTT: poly(2,5-(2-di(thien-2-yl)thieno[3,2-b]thiophene. [c] PCPDTBT: poly(2,6-(4,4-bis(2-ethylhexyl)-4H-cyclopenta[2,1-b;3,4-b′]dithiophene)-alt-4′,7′-(2′,1′,3′-benzothiadiazole. [d] P3HT: poly(3-n-hexylthiophene). [e] SOHEL: self-organized hole extraction layer. [f] PEDOT:PSS: poly(3,4-ethylenedioxythiophene) polystyrene sulfonate. [g] Spiro-TTB: . [h] Spiro-MeO-TPD:. [i] MeO-TPD:. [J] Sprio-MeO-TAD: 2,20,7,70-tetrakis(N,N0-di-p-methoxyphenylamine)-9,90-spirobifluorene poly[3-(6-trimethylammoniumhexyl)thiophene]. [k] Poly-TPD: poly(N,N'-bis(4-butylphenyl-N,N'-bis(phenyl)benzidine. [l] $PC_{61}BM$: [6,6]-Phenyl C_{61} butyric acid methyl ester. [m] BCP: bathocuproine.

Table 3 HELs for PrSCs and their corresponding IE and device performance.*

Table 4 EELs for PrSCs and their corresponding LUMO level and device performance.

EEL	LUMO of EEL (eV)	Perovskite	CBM of Perovskite (eV)	Offset (eV)	V_{oc} (V)	J_{sc} (mA/cm^2)	FF (%)	PCE (%)	Device architecture	Ref
ZnO/$PC_{61}BM$[a]	3.9	$MAPbI_3$	3.7	0.2	1.02	14.73	73	10.87	ITO/EEL/ $MAPbI_3$/PTB7-Th[i]/MoO_3/Ag	160
ZnO	4.2			0.5	0.78	14.54	68	7.65		
$IC_{60}BA$[b]/C_{60}/BCP[c]	3.7	$MAPbI_3$	3.7	0	0.98	11.3	80	8.83	ITO/PEDOT:PSS/ $MAPbI_3$/EEL/Al	22
$PC_{61}BM$/C_{60}/BCP	3.9			0.2	0.82	12.4	74.1	7.53		

*We surveyed relevant articles that compared EELs in PHJ PrSCs and exhibited energy levels of EELs and perovskites and corresponding device performance.
**Regarding EELs used on $PC_{61}BM$ layer, the energy level offset was investigated between $PC_{61}BM$ and electrode.
[a] $PC_{61}BM$: [6,6]-Phenyl C_{61} butyric acid methyl ester. [b] $IC_{60}BA$: indene-C_{60} bisadduct. [c] BCP: bathocuproine. [d] PEIE: poly-(ethyleneimine ethoxylated). [e] P3TMAHT: poly[3-(6-trimethylammoniumhexyl)thiophene]. [f] DMAPA: dimethylaminopropylamine. [g] PDINO: perylene-diimide. [h] TIPD: titanium (diisopropoxide) bis(2,4-pentanedionate). [i] PTB7-Th: Poly[4,8-bis(5-(2-ethylhexyl)thiophen-2-yl)benzo[1,2-b;4,5-b']dithiophene-2,6-diyl-alt-(4-(2-ethylhexyl)-3-fluorothieno[3,4-b]thiophene-)-2-carboxylate-2-6-diyl)].

HTM	IP of HTM (eV)	Perovskite	HOMO of Perovskite (eV)	Offset (eV)	Vo (V
P3HT	5.0	$CH_3NH_3PbI_3$	5.4	0.4	0.7
PCPDTBT	5.0			0.4	0.8
DPP-DTT	5.2			0.2	1.0
PCDTBT	5.3			0.1	1.0
NiOx	5.4	$CH_3NH_3PbI_3$	5.4	0	0.9
PEDOT:PSS	5.1			0.3	0.6

C_{60}/BCP	4.5			0.8	0.53	12.2	33.1	2.14		
PEIE[d]	3.97			0	0.899	17.32	77.10	12.01	ITO/PEDOT:PSS/ $MAPbI_3/PC_{61}BM$/EEL/Ag	146
P3TMAHT[e]	4.13	$MAPbI_{3-x}Cl_x$	4.2**	0.07	0.899	17.10	74.10	11.28		
Ag only	4.7			0.5	0.849	16.00	60.29	8.53		
DMAPA/-C_{60}	3.97	$MAPbI_{3-x}Cl_x$	3.95**	0.02	0.97	17.9	77	13.4	ITO/PEDOT:PSS/ $MAPbI_{3-x}Cl_x/PC_{61}BM$/EEL/Ag	150
Ag only	4.74			0.79	0.90	17.1	61	9.4		
PDINO[g]	3.63			0	0.95	18.8	78.5	14.0		
ZnO	4.4	$MAPbI_{3-x}Cl_x$	3.9**	0.5	0.95	16.0	74.5	11.3	ITO/PEDOT:PSS/ $MAPbI_{3-x}Cl_x$ /$PC_{61}BM$/EEL/Ag	153
Ag only	4.6			0.7	0.85	17.5	67.6	10.0		
TIPD[h]	3.9	$MAPbI_3$	3.9**	0	0.89	22.57	64.5	12.95	ITO/PEDOT:PSS/ $MAPbI_3/PC_{61}BM$/EEL/Al	157
Al only	4.3			0.4	0.83	15.42	67.7	8.66		

However, the difference between the lowest unoccupied molecular orbital (LUMO) of $PC_{61}BM$ and WF of the metal contact causes decrease in quasi-Fermi level difference and lower built-in voltage which lead to low device performance. To form quasi-Ohmic contact between $PC_{61}BM$ and Ag cathode, PEIE or poly[3-(6-trimethylammoniumhexyl)thiophene] (P3TMAHT) were inserted between the layers (Fig. 8c).[146] Both polymers formed interface dipoles with a negative charges on the Ag and decreased its WF from 4.7 eV to 3.97 eV (PEIE) and to 4.13 eV (P3TMAHT). The modifying interfacial layers minimized the energy difference between $PC_{61}BM$ and cathode and maximized the quasi-Fermi level difference in the devices. Hence, V_{oc} increased from 0.85 V to 0.9 V, and J_{sc} and FF were also improved by using the interfacial layers. The device with ITO/PEDOT:PSS/$MAPbI_{3-x}Cl_x$/$PC_{61}BM$/PEIE/Ag achieved PCE = 12.0 %, which was higher than PCE = 8.5 % of the device
that did not have the interfacial layers. Similarly, a chemisorbed dipolar interface layer, DMAPA-C_{60} based on an amine functionalized fullerene derivative was used to make quasi-Ohmic contact between PCBM and Ag cathode in p-i-n PHJ PrSCs.[150] The device structure was ITO/PEDOT:PSS/$MAPbI_{3-x}Cl_x$/$PC_{61}BM$/DMAPA-C_{60}/Ag. Owing to the decreased WF of Ag (3.97 eV) with the interfacial layer, the device achieved PCE = 13.4 % with increased V_{oc} = 0.97 V compared to the device without DMAPA-C_{60} which had PCE = 9.4 % and V_{oc} = 0.9 V.

A thin LiF layer was also used as EEL placed between $PC_{61}BM$ and Al in p-i-n PHJ PrSCs.[147] The function of thin metal fluoride layer in the position has been explained in the field of organic solar cells: 1) formation of a dipole to reduce metal's WF; 2) reaction with metal contact to facilitate charge extraction; and 3) decrease in metal-bonding induced damage to $PC_{61}BM$.[161–164] Based on the effects, devices with LiF/Al showed superior PCE = 13.1 % to PCE of the device without LiF (11.5 %) (Fig. 8d).

In short, V_{oc} strongly depends on the energy level offset at the electrode interfaces. V_{oc} of devices can be increased linearly by using energy-level-tailored HEL and EEL at the interface of PHJ PrSCs. The maximum V_{oc} is achieved when the energy levels of HELs and EELs are pinned to VBM and CBM of perovskite respectively. We expect that this review of how V_{oc} depends on the energy-level tailoring of interfacial layers will be helpful to provide an insight into ways to maximize V_{oc} of devices with various kinds of perovskite light absorbers.

More specific information of the EELs including their characteristics in terms of energy level and device performance are summarized (Table 4).

4.2. Electrical conductivity of interfacial layers

Electrical conductivity of interfacial layers in PHJ PrSCs is also an important factor determining device performance because charge transport occurs through the interfacial layers from perovskite absorbers. In general, high electrical conductivity of an interfacial layer is favourable so that charges can be efficiently collected to a desired electrode with minimized recombination as long as charge balance between electrons and holes are stable in a device. Although spiro-OMeTAD and PTAA are typically used as a hole interfacial layer in n-i-p PHJ PrSCs, they have a low conductivity and low hole mobility in the absence of dopants such as lithium bis(trifluoromethylsulfonyl)-imide (Li-TFSi) and *tert*-butylpyridine (tBP).[165–167] Moreover, the difference in electrical conductivity between perovskite light absorber and an interfacial layer can cause accumulation of charges at the interface and formation of space charges that can impede efficient charge transfer and transport. Therefore, devices with an undoped HEL showed low PCE.[168–172]

To overcome this limitation, a dopant-free donor-acceptor conjugated small molecule, DOR3T-TBDT, was introduced as a HEL in a n-i-p PHJ device with ITO/TiO_2/$MAPbI_{3-x}Cl_x$/DOR3T-TBDT/MoO_3/Ag structure.[81] The bulk electrical conductivity of the HEL measured by a transmission line model at room temperature (*RT*) was ~4 × 10^{-4} S cm^{-1} and the hole mobility extracted from organic field-effect transistors (OFETs) was 0.26 cm^2 $V^{-1}s^{-1}$; both are higher than those of pristine spiro-OMeTAD (conductivity ~10^{-5} S cm^{-2}; hole mobility ~10^{-4} cm^2 $V^{-1}s^{-1}$). Electrochemical impedance spectroscopy (EIS) measurements of devices also showed the lower resistance of the DOR3T-TBDT based device than the device with dopant-free spiro-OMeTAD. Moreover, a significant photoluminescence (PL) quenching and shortened PL lifetime of DOR3T-TBDT interfaced $MAPbI_{3-x}Cl_x$ layer indicated efficient hole extraction. Therefore, the device with DOR3T-TBDT which achieved higher PCE = 14.9 % than PCEs of the devices with dopant-free spiro-OMeTAD (3.5 %).

Another method to increase the low electrical conductivity of pure spiro-OMeTAD is to introduce multi-walled carbon nanotubes (MWNTs) into it.[80] Owing to the high carrier mobility (~220 cm^2 $V^{-1}s^{-1}$), electrical properties of spiro-OMeTAD that incorporated 0.5 wt% of MWNTs had carrier mobility more than two orders of magnitude larger, and conductivity three orders larger than pristine spiro-OMeTAD. Here, however, the lower WF of MWNTs (4.6 eV) provided a path for undesired electron transfer.[173–175] Therefore, a hierarchical structure composed of pure spiro-OMeTAD/spiro-OMeTAD:MWNTs was introduced to block back-electron transfer. The first deposited pure spiro-OMeTAD efficiently blocked back-electron transfer due to its lower LUMO (2.3 eV) than CBM of $MAPbI_3$ (3.9 eV). As a result of increased electrical conductivity of the MWNTs embedded spiro-OMeTAD and efficient blocking of back-electron transfer by pristine spiro-OMeTAD, the device with FTO/TiO_2/$MAPbI_3$/spiro-OMeTAD/spiro-OMeTAD:MWNTs/Au structure achieved PCE = 15.1 % which exceeded the PCE = 12.8 % of the device to which MWNTs were not added.

Studies on EEL of p-i-n PHJ PrSCs have also been reported. PCBM, the popular EEL, has been doped with graphdiyne, a novel two-dimensional carbon material.[155] While the electron mobility of unipolar device with pure PCBM was 2.98 × 10^{-4}

$cm^2\ V^{-1}s^{-1}$, it was increased to 5.32×10^{-4} $cm^2\ V^{-1}s^{-1}$ in the device that used graphdiyne-doped $PC_{61}BM$. The improvement in electron mobility resulted from good electrical characteristics of graphdiyne owing to its carbon network structure with delocalized π-systems. In addition, the device with $PC_{61}BM$:graphdiyne exhibited less charge recombination because of the EEL's better coverage on and interfacial contact with perovskite surface than undoped $PC_{61}BM$. Due to the increased electrical conductivity of the EEL, the device achieved PCE =14.8 %, which was higher than PCE of the device with pristine $PC_{61}BM$ (13.6 %).

The importance of roles of a fullerene-based n-type layer in a p-i-n type PHJ cell was highlighted particularly in respect of electrical conductivity of the materials;[151] the authors presented a clear correlation between the charge-transporting properties of EELs ($IC_{60}BA$, $PC_{61}BM$ and C_{60}) and device performance. Electron mobilities of the fullerene derivatives were obtained from FETs based on each fullerene derivative. The gradual increase in electron mobility from $IC_{60}BA$ (6.9×10^{-3} $cm^2\ V^{-1}s^{-1}$), to $PC_{61}BM$ (6.1×10^{-2} $cm^2\ V^{-1}s^{-1}$), to C_{60} (1.6 $cm^2\ V^{-1}s^{-1}$) was attributed to increased conjugation and dense packing of C_{60} owing to lack of bulky side-chains. For this reason, the device with C_{60} as an ETL achieved the highest J_{sc} = 21.07 mA cm^{-2} and PCE = 15.44 %; the device with $PC_{61}BM$ had J_{sc} = 18.85 mA cm^{-2} and PCE = 13.37 %, and the device with $IC_{60}BA$ had J_{sc} = 11.27 mA cm^{-2} and PCE = 8.06 %. This result indicates that an EEL with good electrical conductivity promotes efficient charge transport in a device and increase its PCE.

4.3 Passivation of traps in perovskites

The presence of a large density of traps in perovskite absorbers has identified as main origin of large photocurrent hysteresis of PrSCs which hampers accurate evaluation of device performance and degrades device reliability.[22,50,51,137,151,176–180] To be specific, the hysteresis comes from the difference in rates of charge trapping and de-trapping according to voltage sweep direction and sweep rate. Therefore, decreasing trap density of states (tDOS) is required to eliminate the hysteresis of a device. One way of decreasing tDOS is to fill or passivate the traps by applying an intimate interfacial layer with perovskite; hysteresis-less PHJ PrSCs have been realized using this approach.[22,50,151]

Huang *et al*. applied a double fullerene layer ($PC_{61}BM/C_{60}$) onto $MAPbI_3$ film.[22] Thermal admittance spectroscopy (TAS) analysis confirmed decrease in tDOS after the interfacial layer passivation on perovskite film. While the device without the interfacial layers had a large tDOS in the range of between 1×10^{17} and 1×10^{19} $m^{-3}\ eV^{-1}$, the device with the interfacial layers had tDOS about two orders of magnitude less than this. tDOS was also significantly mitigated by appropriate thermal annealing on $PC_{61}BM$ (100 °C for 45min) (Fig. 10a).[50] The schematic image in Fig. 10b shows $PC_{61}BM$ passivated the trap states and reduced the surface recombination. The increased surface passivation effect of $PC_{61}BM$ on $MAPbI_3$ was revealed

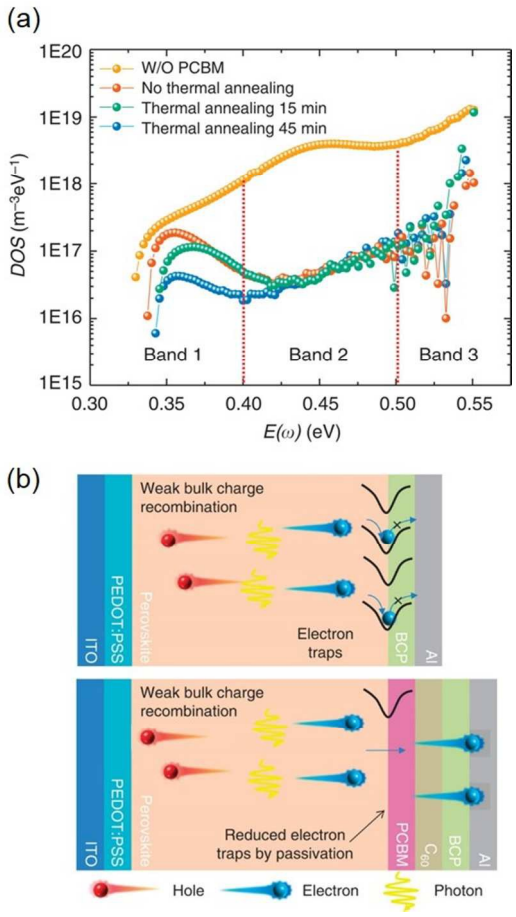

Fig. 10 (a) Trap density of states (tDOS) obtained by thermal admittance spectroscopy. (b) Schematic image of the surface recombination reduction by passivating the trap states. Reproduced from ref. 50 with permission from Nature Publishing Group.

from blue-shift in PL of the films and the surface passivation effect led to reduced interface recombination, increased carrier lifetime and increased mobility, thereby yielding a high PCE around 15 %. The excellence of fullerene derivatives in trap passivation of perovskite in PHJ PrSCs is being reported elsewhere to date.[151]

4.4 Enhancement in long-term stability of devices

Long-term stability of a device is an essential requirement for commercialization. Although PHJ PrSCs have achieved high PCE near 20 %, they have poor long-term stability mainly due to the inherent vulnerability of perovskite light absorbers to moisture and heat. Degradation of perovskite after exposure to moisture and heat can be easily traced in various ways. For example, color change in perovskite film usually from dark brown to yellow, change in the XRD peaks of perovskite crystal structures, and decreased intensity of light absorption are observable.[181–183]

The sensitivity of perovskites to moisture imparts an additional function to interfacial layers. An appropriate choice of interfacial layers to sandwich perovskite can protect it from

exposure to undesirable environments, and thereby extend the stability of a device.

However, the most popular solution-processable conducting polymer HEL in p-i-n PHJ PrSCs, PEDOT:PSS has disadvantages of hygroscopicity and acidity; these properties can degrade the device's long-term stability. Therefore, researchers are seeking a way to improve device stability. Chu *et al*. introduced solution-processable MoO_3 between ITO and PEDOT:PSS, and developed a device that had ITO/MoO_3/PEDOT:PSS/$MAPbI_3$/C_{60}/Bphen/Ag structure.[144] The device showed better long-term stability than the device with only PEDOT:PSS. Metal ions released from ITO due to damage by acidic PEDOT:PSS can diffuse into the inner layer of a device and degrade it. However, insertion of MoO_3 seems to effectively prevent corrosion of ITO by PEDOT:PSS and consequent generation of undesirable species. After 10 days under ambient condition, the PCE of device with the MoO_3 degraded only 7 %, whereas the device with only PEDOT:PSS failed completely. Furthermore, owing to increased hole collection efficiency, the device with MoO_3 showed higher PCE = 12.78 % than the device with only PEDOT:PSS HEL (PCE = 9.81 %). In another approach, PEDOT:PSS was simply replaced with reduced graphene oxide (rGO) nanosheets as a HEL; the replacement increased device stability and PCE at the same time.[88] The basic structure of the devices was ITO/HEL/$MAPbI_3$/$PC_{61}BM$/BCP/Ag. About three times longer half-lifetime of rGO device (~150 h) than the device with PEDOT:PSS (~ 50 h) under ambient condition was attributed to the rGO being nearly neutral properties, unlike PEDOT:PSS, which is acidic. With few surface oxygen functionalities, rGO has inherent passivation ability against moisture and oxygen. Also, the device with rGO achieved PCE = 10.8 %, which was higher than PCE = 9.14 % of the device with PEDOT:PSS. This result was ascribed to the superior charge transport ability due to higher conductivity of rGO than PEDOT:PSS and better-aligned energy levels between rGO and the anode.

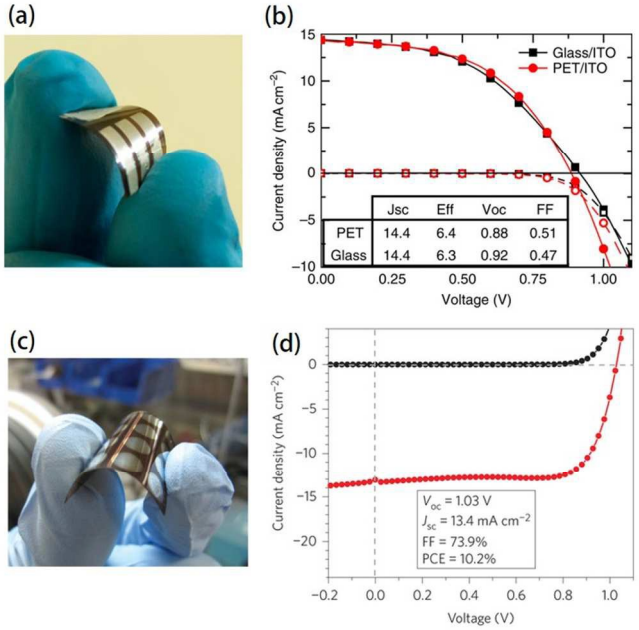

Fig. 11 (a) Picture of flexible p-i-n PHJ PrSCs. (b) *J-V* charateristics of the flexible device and device on glass substrate. Reproduced from ref. 105 with permission from Nature Publishing Group. (c) Picture of flexible n-i-p PHJ PrSCs. (d) *J-V* charateristics measured under illumination (red line) and in the dark (black line). Reproduced from ref. 73 with permission from Nature Publishing Group.

5. Flexible perovskite solar cells

PrSCs are promising candidates as a power sources. Nevertheless, processability at low *T* is an essential requirement for the realization of flexible PrSCs; therefore, PHJ PrSCs are suitable for this purpose.

Snaith *et al*. demonstrated flexible p-i-n PHJ PrSCs on PET/ITO substrates (ITO/PEDOT:PSS/$MAPbI_{3-x}Cl_x$/PCBM/TiO_x/Al);[105] the device had PCE = 6.3 % (Fig. 11a, b). Around the same time, Kelly *et al*. reported flexible n-i-p PHJ PrSCs.[73] The device was completed also on PET/ITO substrate with ITO/ZnO/$MAPbI_3$/spiro-OMeTAD/Ag structure. PCE of the flexible device was 10.2 %. The demonstrations presented development possibility of flexible PHJ PrSCs (Fig. 11c, d).

Jung *et al*. demonstrated bendable n-i-p PHJ PrSCs based on PEN/ITO substrates.[184] The device structure was PEN/ITO/$MAPbI_{3-x}Cl_x$/Sprio-OMeTAD/Ag. The authors investigated bending stability of the device according to bending conditions. The flexible PrSCs showed constant PCE as a function of bending radius r_B from 400 mm to 4 mm. At r_B of 400 mm and 40 mm the devices remained stable, but at r_B of 4 mm the device showed abrupt decrease in PCE after several tens of bending cycles. The authors attributed this decrease to

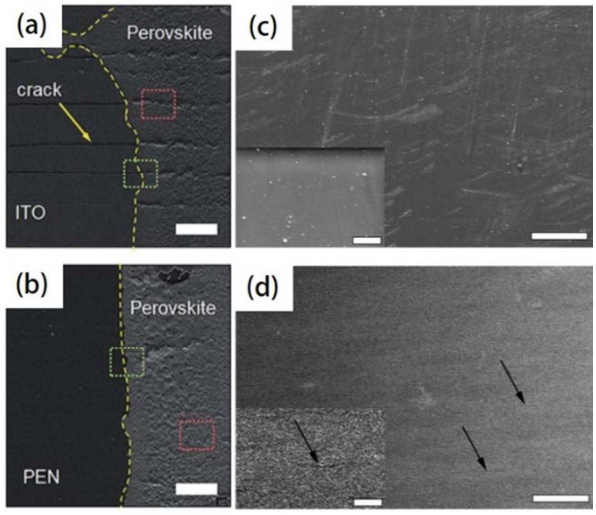

Fig. 12 SEM images of (a) PEN/ITO/TiO_x/perovskite and (b) PEN/TiO_x/perovskite showing perovskite and its junction part after 300 bending cycles. Scale bar represnets 100 μm. Low-magnification and high-magnification (inset) SEM images of (c) PET/highly conductive PEDOT and (d) PET/highly conductive PEDOT/semiconducting PEDOT/perovskite after 2000 bending cycles. (a) and (b) are reproduced from ref. 184 and (c) and (d) are reproduced from ref. 185 with permission from The Royal Society of Chemistry.

brittleness of ITO. Here, the researchers examined fracture behavior of perovskite films. One perovskite film was deposited on PEN/ITO and the other was directly on PEN substrate. The former had cracks from ITO, but the latter did not have any cracks after bending (Fig. 12a, b). The authors attributed this result to the excellent mechanical properties of perovskite film and its compatibility with flexible devices. On the other hand, Kelly *et al*. reported that repeated bending of the device at a low radius (4mm) of curvature caused small cracks in the perovskite films. (Fig. 12c, d).[185] Nevertheless, the authors concluded that perovskite can tolerate moderate conditions such as roll-to-roll manufacturing. Based on these conflicting conclusions, it is worth studying in-depth and further debating on the flexibility and mechanical durability of perovskite films.

The brittleness of FTO and ITO limits the development of flexible PrSCs. Therefore, finding a way to replace the conventional FTO and ITO electrodes with a transparent flexible electrode is a major requirement for development of flexible PrSCs. Although several papers have reported PrSCs that use flexible transparent conducting electrodes (e.g., aluminum-doped ZnO (AZO)/Ag/AZO and PEDOT:PSS) instead of FTO or ITO, PCEs of the flexible devices were lower than rigid devices due to inferior electrical, optical properties of flexible electrodes.[185–187] Therefore, various kinds of flexible transparent conducting electrode (e.g., PEDOT:PSS, graphene,[188,189] carbon nanotubes[189] and silver nanowires[190]) should be vigorously studied with the goal of enhancing compatibility with flexible PrSCs to replace conventional metal oxide brittle electrodes.

6. Conclusions and outlook

We have discussed and pointed out progress in PHJ PrSCs and several strategies for providing insights into interfacial layer engineering to improve photovoltaic performance and stability of PHJ PrSCs.

Importantly, improvement of PCE and stability of PHJ PrSCs requires use of appropriate interfacial layers because the interfacial layers have crucial roles in PHJ PrSCs; 1) proper energy-level tailoring can reduce energy offset between intimate layers, and thereby increase built-in potential, and facilitate charge transfer and extraction; 2) electrical conductivity of the interfacial layers strongly affects property of charge transport and efficiency of charge collection; 3) passivation of electronic trap sites in perovskite film can eliminate photocurrent hysteresis; 4) protection of perovskite from moisture improves long-term stability. On the basis of various functions and optimization with comprehensive understanding of interfacial layers, PHJ PrSCs are expected to be further improved in PCE and long-term stability. Obviously, to develop highly efficient flexible PHJ PrSCs, we also need to understand failure mechanism of the devices against mechanical stress, and adopt a transparent conducting flexible electrode that has excellent electrical, optical, and mechanical properties.

Because one of the ultimate goals of research on PrSCs is to make it ubiquitous in everyday life, manufacturing cost in addition to flexibility should be considered. To meet these requirements, we suggest that p-i-n type PHJ PrSCs are more promising than n-i-p type, because the structure of, p-i-n type PHJ PrSCs can be further simplified. Specifically, PEDOT:PSS, a representative HEL for p-i-n type PHJ PrSCs, can be modified to have great electrical conductivity (~ 4000 S/cm)[193] and a wide range of WF (4.8 ~ 5.9 eV)[6,141,194] by appropriate chemical treatment. With this adjustability, PEDOT:PSS can concurrently perform both charge extraction and collection in a simple integrated single layer in p-i-n type PHJ PrSCs. Secondly, an all-solution-processed flexible PrSCs is achievable because PEDOT:PSS is solution processable and a film of PEDOT:PSS is flexible, whereas conventional metal oxide electrodes (e.g., ITO and FTO) are fabricated by vacuum processing, and are brittle. Therefore, flexible p-i-n type PHJ PrSCs can be fabricated by all-solution roll-to-roll processing. In summary, we expect that a p-i-n type PHJ PrSCs can have advantages of structure and processing over n-i-p type, and that these advantages will lead to cost-effective fabrication and wide use. However, the stability of PEDOT:PSS is a critical limitation. We believe that this problem can be solved by using types of fluorinated conducting polymers.[6,141,194,195]

Acknowledgements

This work was supported by the Center for Advanced Soft-Electronics funded by the Ministry of Science, ICT and Future Planning as Global Frontier Project (CASE-2014M3A6A5060947). This work was also supported by POSCO.

Notes

Department of Materials Science and Engineering, Pohang University of Science and Technology (POSTECH), Pohang 790-784, Republic of Korea. E-mail: twlee@postech.ac.kr, taewlees@gmail.com

† These authors contributed equally to this work.

References

1 H.-S. Kim, C.-R. Lee, J.-H. Im, K.-B. Lee, T. Moehl, A. Marchioro, S.-J. Moon, R. Humphry-Baker, J.-H. Yum, J. E. Moser, M. Grätzel and N.-G. Park, *Sci. Rep.*, 2012, **2**, 591.

2 S. D. Stranks, G. E. Eperon, G. Grancini, C. Menelaou, M. J. P. Alcocer, T. Leijtens, L. M. Herz, A. Petrozza and H. J. Snaith, *Science*, 2013, **342** , 341–344.

3 J. Burschka, N. Pellet, S.-J. Moon, R. Humphry-Baker, P. Gao, M. K. Nazeeruddin, M. Grätzel and M. Gratzel, *Nature*, 2013, **499**, 316–319.

4 W. S. Yang, J. H. Noh, N. J. Jeon, Y. C. Kim, S. Ryu, J. Seo and S. Il Seok, *Science*, 2015, **348** , 1234–1237.

5 Z.-K. Tan, R. S. Moghaddam, M. L. Lai, P. Docampo, R. Higler, F. Deschler, M. Price, A. Sadhanala, L. M. Pazos, D. Credgington, F. Hanusch, T. Bein, H. J. Snaith and R. H. Friend, *Nat. Nanotechnol.*, 2014, **9**, 687–692.

6 Y.-H. Kim, H. Cho, J. H. Heo, T.-S. Kim, N. Myoung, C.-L. Lee, S. H. Im and T.-W. Lee, *Adv. Mater.*, 2015, **27**, 1248–1254.
7 J. C. Yu, D. Bin Kim, G. Baek, B. R. Lee, E. D. Jung, S. Lee, J. H. Chu, D.-K. Lee, K. J. Choi, S. Cho and M. H. Song, *Adv. Mater.*, 2015, **27**, 3492–3500.
8 L. Dou, Y. (Micheal) Yang, J. You, Z. Hong, W.-H. Chang, G. Li and Y. Yang, *Nat. Commun.*, 2014, **5**, 5404.
9 Y. Lee, J. Kwon, E. Hwang, C.-H. Ra, W. J. Yoo, J.-H. Ahn, J. H. Park and J. H. Cho, *Adv. Mater.*, 2015, **27**, 41–46.
10 Q. Lin, A. Armin, D. M. Lyons, P. L. Burn and P. Meredith, *Adv. Mater.*, 2015, **27**, 2060–2064.
11 H. Zhu, Y. Fu, F. Meng, X. Wu, Z. Gong, Q. Ding, M. V Gustafsson, M. T. Trinh, S. Jin and X.-Y. Zhu, *Nat. Mater.*, 2015, **14**, 636–642.
12 F. Deschler, M. Price, S. Pathak, L. E. Klintberg, D.-D. Jarausch, R. Higler, S. Hüttner, T. Leijtens, S. D. Stranks, H. J. Snaith, M. Atatüre, R. T. Phillips and R. H. Friend, *J. Phys. Chem. Lett.*, 2014, **5**, 1421–1426.
13 G. Xing, N. Mathews, S. S. Lim, N. Yantara, X. Liu, D. Sabba, M. Grätzel, S. Mhaisalkar and T. C. Sum, *Nat. Mater.*, 2014, **13**, 476–480.
14 A. Kojima, K. Teshima, Y. Shirai and T. Miyasaka, *J. Am. Chem. Soc.*, 2009, **131**, 6050–6051.
15 B. O'Regan and M. Gratzel, *Nature*, 1991, **353**, 737–740.
16 Y.-H. Kim, I.-K. Lee, Y.-S. Song, M.-H. Lee, B.-Y. Kim, N.-I. Cho and D. Lee, *Electron. Mater. Lett.*, 2014, **10**, 445–449.
17 J. Park and M. Lee, *Electron. Mater. Lett.*, 2015, **11**, 271–275.
18 J.-H. Im, C.-R. Lee, J.-W. Lee, S.-W. Park and N.-G. Park, *Nanoscale*, 2011, **3**, 4088–4093.
19 H. Zhou, Q. Chen, G. Li, S. Luo, T. Song, H.-S. Duan, Z. Hong, J. You, Y. Liu and Y. Yang, *Science*, 2014, **345** , 542–546.
20 P.-W. Liang, C.-Y. Liao, C.-C. Chueh, F. Zuo, S. T. Williams, X.-K. Xin, J. Lin and A. K.-Y. Jen, *Adv. Mater.*, 2014, **26**, 3748–3754.
21 Z. Xiao, C. Bi, Y. Shao, Q. Dong, Q. Wang, Y. Yuan, C. Wang, Y. Gao and J. Huang, *Energy Environ. Sci.*, 2014, **7**, 2619–2623.
22 Q. Wang, Y. Shao, Q. Dong, Z. Xiao, Y. Yuan and J. Huang, *Energy Environ. Sci.*, 2014, **7**, 2359–2365.
23 C.-C. Chueh, C.-Y. Liao, F. Zuo, S. T. Williams, P.-W. Liang and A. K.-Y. Jen, *J. Mater. Chem. A*, 2015, **3**, 9058–9062.
24 C. Bi, Y. Shao, Y. Yuan, Z. Xiao, C. Wang, Y. Gao and J. Huang, *J. Mater. Chem. A*, 2014, **2**, 18508–18514.
25 Z. Xiao, Q. Dong, C. Bi, Y. Shao, Y. Yuan and J. Huang, *Adv. Mater.*, 2014, **26**, 6503–6509.
26 C. Zuo and L. Ding, *Nanoscale*, 2014, **6**, 9935–9938.
27 H.-B. Kim, H. Choi, J. Jeong, S. Kim, B. Walker, S. Song and J. Y. Kim, *Nanoscale*, 2014, **6**, 6679–6683.
28 H.-L. Hsu, C.-P. Chen, J.-Y. Chang, Y.-Y. Yu and Y.-K. Shen, *Nanoscale*, 2014, **6**, 10281–10288.
29 J. W. Jung, S. T. Williams and A. K.-Y. Jen, *RSC Adv.*, 2014, **4**, 62971–62977.
30 F. X. Xie, D. Zhang, H. Su, X. Ren, K. S. Wong, M. Grätzel and W. C. H. Choy, *ACS Nano*, 2015, **9**, 639–646.
31 P.-W. Liang, C.-C. Chueh, X.-K. Xin, F. Zuo, S. T. Williams, C.-Y. Liao and A. K.-Y. Jen, *Adv. Energy Mater.*, 2015, **5**, 1400960.
32 Y. Chen, T. Chen and L. Dai, *Adv. Mater.*, 2015, **27**, 1053–1059.
33 X. Song, W. Wang, P. Sun, W. Ma and Z.-K. Chen, *Appl. Phys. Lett.*, 2015, **106**, 033901.
34 H.-L. Hsu, C.-C. Chang, C.-P. Chen, B.-H. Jiang, R.-J. Jeng and C.-H. Cheng, *J. Mater. Chem. A*, 2015, **3**, 9271–9277.
35 T.-B. Song, Q. Chen, H. Zhou, S. Luo, Y. (Michael) Yang, J. You and Y. Yang, *Nano Energy*, 2015, **12**, 494–500.
36 D. Wang, Z. Liu, Z. Zhou, H. Zhu, Y. Zhou, C. Huang, Z. Wang, H. Xu, Y. Jin, B. Fan, S. Pang and G. Cui, *Chem. Mater.*, 2014, **26**, 7145–7150.
37 R. Kang, J.-E. Kim, J.-S. Yeo, S. Lee, Y.-J. Jeon and D.-Y. Kim, *J. Phys. Chem. C*, 2014, **118**, 26513–26520.
38 Y. Chen, Y. Zhao and Z. Liang, *Chem. Mater.*, 2015, **27**, 1448–1451.
39 L. Q. Zhang, X. W. Zhang, Z. G. Yin, Q. Jiang, X. Liu, J. H. Meng, Y. J. Zhao and H. L. Wang, *J. Mater. Chem. A*, 2015, **3**, 12133–12138.
40 J. Lian, Q. Wang, Y. Yuan, Y. Shao and J. Huang, *J. Mater. Chem. A*, 2015, **3**, 9146–9151.
41 K. Wang, C. Liu, P. Du, L. Chen, J. Zhu, A. Karim and X. Gong, *Org. Electron.*, 2015, **21**, 19–26.
42 J. Xiong, B. Yang, R. Wu, C. Cao, Y. Huang, C. Liu, Z. Hu, H. Huang, Y. Gao and J. Yang, *Org. Electron.*, 2015, **24**, 106–112.
43 X. Wang, X. Li, G. Tang, L. Zhao, W. Zhang, T. Jiu and J. Fang, *Org. Electron.*, 2015, **24**, 205–211.
44 Z. Liu and E.-C. Lee, *Org. Electron.*, 2015, **24**, 101–105.
45 K. Wang, C. Liu, P. Du, H.-L. Zhang and X. Gong, *Small*, 2015, DOI: 10.1002/smll.201403399.
46 W. Nie, H. Tsai, R. Asadpour, J.-C. Blancon, A. J. Neukirch, G. Gupta, J. J. Crochet, M. Chhowalla, S. Tretiak, M. A. Alam, H.-L. Wang and A. D. Mohite, *Science*, 2015, **347** , 522–525.
47 P. Schulz, E. Edri, S. Kirmayer, G. Hodes, D. Cahen and A. Kahn, *Energy Environ. Sci.*, 2014, **7**, 1377–1381.
48 Q.-K. Wang, R.-B. Wang, P.-F. Shen, C. Li, Y.-Q. Li, L.-J. Liu, S. Duhm and J.-X. Tang, *Adv. Mater. Interfaces*, 2015, **2**, 1400528.
49 P. Schulz, L. L. Whittaker-Brooks, B. A. MacLeod, D. C. Olson, Y.-L. Loo and A. Kahn, *Adv. Mater. Interfaces*, 2015, **2**, 1400532.
50 Y. Shao, Z. Xiao, C. Bi, Y. Yuan and J. Huang, *Nat. Commun.*, 2014, **5**, 5784.
51 N. K. Noel, A. Abate, S. D. Stranks, E. S. Parrott, V. M. Burlakov, A. Goriely and H. J. Snaith, *ACS Nano*, 2014, **8**, 9815–9821.
52 T. Leijtens, S. D. Stranks, G. E. Eperon, R. Lindblad, E. M. J. Johansson, I. J. McPherson, H. Rensmo, J. M. Ball, M. M. Lee and H. J. Snaith, *ACS Nano*, 2014, **8**, 7147–7155.
53 A. Baumann, S. Väth, P. Rieder, M. C. Heiber, K. Tvingstedt and V. Dyakonov, *J. Phys. Chem. Lett.*, 2015, **6**, 2350–2354.
54 G.-J. A. H. Wetzelaer, M. Scheepers, A. M. Sempere, C. Momblona, J. Ávila and H. J. Bolink, *Adv. Mater.*, 2015, **27**, 1837–1841.
55 D. B. Mitzi, C. A. Feild, W. T. A. Harrison and A. M. Guloy, *Nature*, 1994, **369**, 467–469.
56 V. M. Goldschmidt, *Naturwissenschaften*, 1926, **14**, 477–485.
57 C. Li, X. Lu, W. Ding, L. Feng, Y. Gao and Z. Guo, *Acta Crystallogr. Sect. B*, 2008, **64**, 702–707.
58 K. Tanaka, T. Takahashi, T. Ban, T. Kondo, K. Uchida and N. Miura, *Solid State Commun.*, 2003, **127**, 619–623.
59 M. Hirasawa, T. Ishihara, T. Goto, K. Uchida and N. Miura, *Phys. B Condens. Matter*, 1994, **201**, 427–430.
60 T. Ishihara, *J. Lumin.*, 1994, **60–61**, 269–274.
61 I. B. K. and L. D. and G. C. Papavassiliou, *J. Phys. Condens. Matter*, 1996, **8**, 1217.
62 W. Zhang, M. Saliba, S. D. Stranks, Y. Sun, X. Shi, U. Wiesner and H. J. Snaith, *Nano Lett.*, 2013, **13**, 4505–4510.
63 V. D'Innocenzo, G. Grancini, M. J. P. Alcocer, A. R. S. Kandada, S. D. Stranks, M. M. Lee, G. Lanzani, H. J. Snaith and A. Petrozza, *Nat. Commun.*, 2014, **5**, 3586.

64 Q. Lin, A. Armin, R. C. R. Nagiri, P. L. Burn and P. Meredith, *Nat. Photonics*, 2015, **9**, 106–112.
65 J. H. Heo, S. H. Im, J. H. Noh, T. N. Mandal, C.-S. Lim, J. A. Chang, Y. H. Lee, H. Kim, A. Sarkar, N. K., M. Gratzel and S. Il Seok, *Nat. Photonics*, 2013, **7**, 486–491.
66 H. J. Snaith, *J. Phys. Chem. Lett.*, 2013, **4**, 3623–3630.
67 N. J. Jeon, J. H. Noh, Y. C. Kim, W. S. Yang, S. Ryu and S. Il Seok, *Nat. Mater.*, 2014, **13**, 897–903.
68 J. M. Ball, M. M. Lee, A. Hey and H. J. Snaith, *Energy Environ. Sci.*, 2013, **6**, 1739–1743.
69 D. Liu, M. K. Gangishetty and T. L. Kelly, *J. Mater. Chem. A*, 2014, **2**, 19873–19881.
70 B. Conings, L. Baeten, T. Jacobs, R. Dera, J. D'Haen, J. Manca and H.-G. Boyen, *APL Mater.*, 2014, **2**, 081505.
71 J. Song, E. Zheng, J. Bian, X.-F. Wang, W. Tian, Y. Sanehira and T. Miyasaka, *J. Mater. Chem. A*, 2015, **3**, 10837–10844.
72 C.-Y. Chang, C.-Y. Chu, Y.-C. Huang, C.-W. Huang, S.-Y. Chang, C.-A. Chen, C.-Y. Chao and W.-F. Su, *ACS Appl. Mater. Interfaces*, 2015, **7**, 4955–4961.
73 D. Liu and T. L. Kelly, *Nat. Photonics*, 2014, **8**, 133–138.
74 L. Wang, W. Fu, Z. Gu, C. Fan, X. Yang, H. Li and H. Chen, *J. Mater. Chem. C*, 2014, **2**, 9087–9090.
75 S. Ryu, J. Seo, S. S. Shin, Y. C. Kim, N. J. Jeon, J. H. Noh and S. Il Seok, *J. Mater. Chem. A*, 2015, **3**, 3271–3275.
76 H.-H. Wang, Q. Chen, H. Zhou, L. Song, Z. S. Louis, N. De Marco, Y. Fang, P. Sun, T.-B. Song, H. Chen and Y. Yang, *J. Mater. Chem. A*, 2015, **3**, 9108–9115.
77 H. Zhou, Y. Shi, K. Wang, Q. Dong, X. Bai, Y. Xing, Y. Du and T. Ma, *J. Phys. Chem. C*, 2015, **119**, 4600–4605.
78 A. Yella, L.-P. Heiniger, P. Gao, M. K. Nazeeruddin and M. Grätzel, *Nano Lett.*, 2014, **14**, 2591–2596.
79 K. Wang, Y. Shi, Q. Dong, Y. Li, S. Wang, X. Yu, M. Wu and T. Ma, *J. Phys. Chem. Lett.*, 2015, **6**, 755–759.
80 J. Lee, M. M. Menamparambath, J.-Y. Hwang and S. Baik, *ChemSusChem*, 2015, DOI: 10.1002/cssc.201403462.
81 Y. Liu, Q. Chen, H.-S. Duan, H. Zhou, Y. (Michael) Yang, H. Chen, S. Luo, T.-B. Song, L. Dou, Z. Hong and Y. Yang, *J. Mater. Chem. A*, 2015, **3**, 11940–11947.
82 L. Zuo, Z. Gu, T. Ye, W. Fu, G. Wu, H. Li and H. Chen, *J. Am. Chem. Soc.*, 2015, **137**, 2674–2679.
83 J.-Y. Jeng, Y.-F. Chiang, M.-H. Lee, S.-R. Peng, T.-F. Guo, P. Chen and T.-C. Wen, *Adv. Mater.*, 2013, **25**, 3727–3732.
84 L. Etgar, P. Gao, Z. Xue, Q. Peng, A. K. Chandiran, B. Liu, M. K. Nazeeruddin and M. Grätzel, *J. Am. Chem. Soc.*, 2012, **134**, 17396–17399.
85 K.-C. Wang, J.-Y. Jeng, P.-S. Shen, Y.-C. Chang, E. W.-G. Diau, C.-H. Tsai, T.-Y. Chao, H.-C. Hsu, P.-Y. Lin, P. Chen, T.-F. Guo and T.-C. Wen, *Sci. Rep.*, 2014, **4**, 4756.
86 S. Ye, W. Sun, Y. Li, W. Yan, H. Peng, Z. Bian, Z. Liu and C. Huang, *Nano Lett.*, 2015, **15**, 3723–3728.
87 Z. Wu, S. Bai, J. Xiang, Z. Yuan, Y. Yang, W. Cui, X. Gao, Z. Liu, Y. Jin and B. Sun, *Nanoscale*, 2014, **6**, 10505–10510.
88 J.-S. Yeo, R. Kang, S. Lee, Y.-J. Jeon, N. Myoung, C.-L. Lee, D.-Y. Kim, J.-M. Yun, Y.-H. Seo, S.-S. Kim and S.-I. Na, *Nano Energy*, 2015, **12**, 96–104.
89 B. Conings, L. Baeten, C. De Dobbelaere, J. D'Haen, J. Manca and H.-G. Boyen, *Adv. Mater.*, 2014, **26**, 2041–2046.
90 Q. Chen, H. Zhou, Z. Hong, S. Luo, H.-S. Duan, H.-H. Wang, Y. Liu, G. Li and Y. Yang, *J. Am. Chem. Soc.*, 2014, **136**, 622–625.
91 G. E. Eperon, S. D. Stranks, C. Menelaou, M. B. Johnston, L. M. Herz and H. J. Snaith, *Energy Environ. Sci.*, 2014, **7**, 982–988.
92 M. Xiao, F. Huang, W. Huang, Y. Dkhissi, Y. Zhu, J. Etheridge, A. Gray-Weale, U. Bach, Y.-B. Cheng and L. Spiccia, *Angew. Chemie*, 2014, **126**, 10056–10061.
93 Y. Wu, A. Islam, X. Yang, C. Qin, J. Liu, K. Zhang, W. Peng and L. Han, *Energy Environ. Sci.*, 2014, **7**, 2934–2938.
94 J. H. Heo, D. H. Song and S. H. Im, *Adv. Mater.*, 2014, **26**, 8179–8183.
95 P. Docampo, F. C. Hanusch, S. D. Stranks, M. Döblinger, J. M. Feckl, M. Ehrensperger, N. K. Minar, M. B. Johnston, H. J. Snaith and T. Bein, *Adv. Energy Mater.*, 2014, **4**, 1400355.
96 Y. Zhao and K. Zhu, *J. Am. Chem. Soc.*, 2014, **136**, 12241–12244.
97 Y. Guo, C. Liu, K. Inoue, K. Harano, H. Tanaka and E. Nakamura, *J. Mater. Chem. A*, 2014, **2**, 13827–13830.
98 M. Saliba, K. W. Tan, H. Sai, D. T. Moore, T. Scott, W. Zhang, L. A. Estroff, U. Wiesner and H. J. Snaith, *J. Phys. Chem. C*, 2014, **118**, 17171–17177.
99 F. C. Hanusch, E. Wiesenmayer, E. Mankel, A. Binek, P. Angloher, C. Fraunhofer, N. Giesbrecht, J. M. Feckl, W. Jaegermann, D. Johrendt, T. Bein and P. Docampo, *J. Phys. Chem. Lett.*, 2014, **5**, 2791–2795.
100 Q. Chen, H. Zhou, T.-B. Song, S. Luo, Z. Hong, H.-S. Duan, L. Dou, Y. Liu and Y. Yang, *Nano Lett.*, 2014, **14**, 4158–4163.
101 Z. Ren, A. Ng, Q. Shen, H. C. Gokkaya, J. Wang, L. Yang, W.-K. Yiu, G. Bai, A. B. Djurišić, W. W. Leung, J. Hao, W. K. Chan and C. Surya, *Sci. Rep.*, 2014, **4**, 6752.
102 J. H. Heo, D. H. Song, H. J. Han, S. Y. Kim, J. H. Kim, D. Kim, H. W. Shin, T. K. Ahn, C. Wolf, T.-W. Lee and S. H. Im, *Adv. Mater.*, 2015, **27**, 3424–3430.
103 Y. Zhou, M. Yang, W. Wu, A. L. Vasiliev, K. Zhu and N. P. Padture, *J. Mater. Chem. A*, 2015, **3**, 8178–8184.
104 W. Zhang, M. Saliba, D. T. Moore, S. K. Pathak, M. T. Hörantner, T. Stergiopoulos, S. D. Stranks, G. E. Eperon, J. A. Alexander-Webber, A. Abate, A. Sadhanala, S. Yao, Y. Chen, R. H. Friend, L. A. Estroff, U. Wiesner and H. J. Snaith, *Nat. Commun.*, 2015, **6**, 6142.
105 P. Docampo, J. M. Ball, M. Darwich, G. E. Eperon and H. J. Snaith, *Nat. Commun.*, 2013, **4**, 2761.
106 J. You, Z. Hong, Y. (Michael) Yang, Q. Chen, M. Cai, T.-B. Song, C.-C. Chen, S. Lu, Y. Liu, H. Zhou and Y. Yang, *ACS Nano*, 2014, **8**, 1674–1680.
107 J. You, Y. (Michael) Yang, Z. Hong, T.-B. Song, L. Meng, Y. Liu, C. Jiang, H. Zhou, W.-H. Chang, G. Li and Y. Yang, *Appl. Phys. Lett.*, 2014, **105**, 183902.
108 C.-H. Chiang, Z.-L. Tseng and C.-G. Wu, *J. Mater. Chem. A*, 2014, **2**, 15897–15903.
109 Y. Rong, Z. Tang, Y. Zhao, X. Zhong, S. Venkatesan, H. Graham, M. Patton, Y. Jing, A. M. Guloy and Y. Yao, *Nanoscale*, 2015, **7**, 10595–10599.
110 Q. Xue, Z. Hu, C. Sun, Z. Chen, F. Huang, H.-L. Yip and Y. Cao, *RSC Adv.*, 2015, **5**, 775–783.
111 F. Zuo, S. T. Williams, P.-W. Liang, C.-C. Chueh, C.-Y. Liao and A. K.-Y. Jen, *Adv. Mater.*, 2014, **26**, 6454–6460.
112 H. Choi, J. Jeong, H.-B. Kim, S. Kim, B. Walker, G.-H. Kim and J. Y. Kim, *Nano Energy*, 2014, **7**, 80–85.
113 Z. Cheng and J. Lin, *CrystEngComm*, 2010, **12**, 2646–2662.
114 J. H. Noh, S. H. Im, J. H. Heo, T. N. Mandal and S. Il Seok, *Nano Lett.*, 2013, **13**, 1764–1769.
115 J. A. Christians, P. A. Miranda Herrera and P. V Kamat, *J. Am. Chem. Soc.*, 2015, **137**, 1530–1538.
116 J. M. Frost, K. T. Butler, F. Brivio, C. H. Hendon, M. van Schilfgaarde and A. Walsh, *Nano Lett.*, 2014, **14**, 2584–2590.
117 M. Liu, M. B. Johnston and H. J. Snaith, *Nature*, 2013, **501**, 395–398.

118 O. Malinkiewicz, A. Yella, Y. H. Lee, G. M. Espallargas, M. Graetzel, M. K. Nazeeruddin and H. J. Bolink, *Nat. Photonics*, 2014, **8**, 128–132.
119 L. E. Polander, P. Pahner, M. Schwarze, M. Saalfrank, C. Koerner and K. Leo, *APL Mater.*, 2014, **2**, 081503.
120 T.-W. Lee, T. Noh, H.-W. Shin, O. Kwon, J.-J. Park, B.-K. Choi, M.-S. Kim, D. W. Shin and Y.-R. Kim, *Adv. Funct. Mater.*, 2009, **19**, 1625–1630.
121 B.-S. Kim, T.-M. Kim, M.-S. Choi, H.-S. Shim and J.-J. Kim, *Org. Electron.*, 2015, **17**, 102–106.
122 T.-W. Lee, K.-G. Lim and D.-H. Kim, *Electron. Mater. Lett.*, 2010, **6**, 41–50.
123 J. H. Park, T.-W. Lee, B.-D. Chin, D. H. Wang and O. O. Park, *Macromol. Rapid Commun.*, 2010, **31**, 2095–2108.
124 D.-H. Kim, K.-G. Lim, J. H. Park and T.-W. Lee, *ChemSusChem*, 2012, **5**, 2053–2057.
125 S. D. Stranks, V. M. Burlakov, T. Leijtens, J. M. Ball, A. Goriely and H. J. Snaith, *Phys. Rev. Appl.*, 2014, **2**, 034007.
126 E. Edri, S. Kirmayer, D. Cahen and G. Hodes, *J. Phys. Chem. Lett.*, 2013, **4**, 897–902.
127 D. Bi, S.-J. Moon, L. Haggman, G. Boschloo, L. Yang, E. M. J. Johansson, M. K. Nazeeruddin, M. Gratzel and A. Hagfeldt, *RSC Adv.*, 2013, **3**, 18762–18766.
128 S. Ryu, J. H. Noh, N. J. Jeon, Y. Chan Kim, W. S. Yang, J. Seo and S. Il Seok, *Energy Environ. Sci.*, 2014, **7**, 2614–2618.
129 B. Cai, Y. Xing, Z. Yang, W.-H. Zhang and J. Qiu, *Energy Environ. Sci.*, 2013, **6**, 1480–1485.
130 L. Yang, U. B. Cappel, E. L. Unger, M. Karlsson, K. M. Karlsson, E. Gabrielsson, L. Sun, G. Boschloo, A. Hagfeldt and E. M. J. Johansson, *Phys. Chem. Chem. Phys.*, 2012, **14**, 779–789.
131 C. Liu, K. Wang, P. Du, T. Meng, X. Yu, S. Z. D. Cheng and X. Gong, *ACS Appl. Mater. Interfaces*, 2015, **7**, 1153–1159.
132 A. T. Barrows, A. J. Pearson, C. K. Kwak, A. D. F. Dunbar, A. R. Buckley and D. G. Lidzey, *Energy Environ. Sci.*, 2014, **7**, 2944–2950.
133 S. Sun, T. Salim, N. Mathews, M. Duchamp, C. Boothroyd, G. Xing, T. C. Sum and Y. M. Lam, *Energy Environ. Sci.*, 2014, **7**, 399–407.
134 S. Paek, N. Cho, H. Choi, H. Jeong, J. S. Lim, J.-Y. Hwang, J. K. Lee and J. Ko, *J. Phys. Chem. C*, 2014, **118**, 25899–25905.
135 J. H. Kim, S. T. Williams, N. Cho, C.-C. Chueh and A. K.-Y. Jen, *Adv. Energy Mater.*, 2015, **5**, 1401229.
136 M. Ramesh, K. M. Boopathi, T.-Y. Huang, Y.-C. Huang, C.-S. Tsao and C.-W. Chu, *ACS Appl. Mater. Interfaces*, 2015, **7**, 2359–2366.
137 J. H. Heo, H. J. Han, D. Kim, T. K. Ahn and S. H. Im, *Energy Environ. Sci.*, 2015, **8**, 1602–1608.
138 N. Tripathi, M. Yanagida, Y. Shirai, T. Masuda, L. Han and K. Miyano, *J. Mater. Chem. A*, 2015, **3**, 12081–12088.
139 K. M. Boopathi, M. Ramesh, P. Perumal, Y.-C. Huang, C.-S. Tsao, Y.-F. Chen, C.-H. Lee and C.-W. Chu, *J. Mater. Chem. A*, 2015, **3**, 9257–9263.
140 H.-L. Hsu, T.-Y. Juang, C.-P. Chen, C.-M. Hsieh, C.-C. Yang, C.-L. Huang and R.-J. Jeng, *Sol. Energy Mater. Sol. Cells*, 2015, **140**, 224–231.
141 K.-G. Lim, H.-B. Kim, J. Jeong, H. Kim, J. Y. Kim and T.-W. Lee, *Adv. Mater.*, 2014, **26**, 6461–6466.
142 W. Yan, Y. Li, W. Sun, H. Peng, S. Ye, Z. Liu, Z. Bian and C. Huang, *RSC Adv.*, 2014, **4**, 33039–33046.
143 D. Zhao, M. Sexton, H.-Y. Park, G. Baure, J. C. Nino and F. So, *Adv. Energy Mater.*, 2015, **5**, 1401855.
144 F. Hou, Z. Su, F. Jin, X. Yan, L. Wang, H. Zhao, J. Zhu, B. Chu and W. Li, *Nanoscale*, 2015, **7**, 9427–9432.
145 M. Qian, M. Li, X.-B. Shi, H. Ma, Z.-K. Wang and L.-S. Liao, *J. Mater. Chem. A*, 2015, **3**, 13533–13539.
146 H. Zhang, H. Azimi, Y. Hou, T. Ameri, T. Przybilla, E. Spiecker, M. Kraft, U. Scherf and C. J. Brabec, *Chem. Mater.*, 2014, **26**, 5190–5193.
147 J. Seo, S. Park, Y. Chan Kim, N. J. Jeon, J. H. Noh, S. C. Yoon and S. Il Seok, *Energy Environ. Sci.*, 2014, **7**, 2642–2646.
148 Q. Xue, Z. Hu, J. Liu, J. Lin, C. Sun, Z. Chen, C. Duan, J. Wang, C. Liao, W. M. Lau, F. Huang, H.-L. Yip and Y. Cao, *J. Mater. Chem. A*, 2014, **2**, 19598–19603.
149 W. Wang, J. Yuan, G. Shi, X. Zhu, S. Shi, Z. Liu, L. Han, H.-Q. Wang and W. Ma, *ACS Appl. Mater. Interfaces*, 2015, **7**, 3994–3999.
150 H. Azimi, T. Ameri, H. Zhang, Y. Hou, C. O. R. Quiroz, J. Min, M. Hu, Z.-G. Zhang, T. Przybilla, G. J. Matt, E. Spiecker, Y. Li and C. J. Brabec, *Adv. Energy Mater.*, 2015, **5**, 1401692.
151 P.-W. Liang, C.-C. Chueh, S. T. Williams and A. K.-Y. Jen, *Adv. Energy Mater.*, 2015, **5**, DOI: 10.1002/aenm.201402321.
152 H. Dong, Z. Wu, B. Xia, J. Xi, F. Yuan, S. Ning, L. Xiao and X. Hou, *Chem. Commun.*, 2015, **51**, 8986–8989.
153 J. Min, Z.-G. Zhang, Y. Hou, C. O. Ramirez Quiroz, T. Przybilla, C. Bronnbauer, F. Guo, K. Forberich, H. Azimi, T. Ameri, E. Spiecker, Y. Li and C. J. Brabec, *Chem. Mater.*, 2015, **27**, 227–234.
154 X. Liu, W. Jiao, M. Lei, Y. Zhou, B. Song and Y. Li, *J. Mater. Chem. A*, 2015, **3**, 9278–9284.
155 C. Kuang, G. Tang, T. Jiu, H. Yang, H. Liu, B. Li, W. Luo, X. Li, W. Zhang, F. Lu, J. Fang and Y. Li, *Nano Lett.*, 2015, **15**, 2756–2762.
156 K. Sun, J. Chang, F. H. Isikgor, P. Li and J. Ouyang, *Nanoscale*, 2015, **7**, 896–900.
157 C. Li, F. Wang, J. Xu, J. Yao, B. Zhang, C. Zhang, M. Xiao, S. Dai, Y. Li and Z. Tan, *Nanoscale*, 2015, **7**, 9771–9778.
158 C. Sun, Q. Xue, Z. Hu, Z. Chen, F. Huang, H.-L. Yip and Y. Cao, *Small*, 2015, DOI: 10.1002/smll.201403344.
159 O. Malinkiewicz, C. Roldán-Carmona, A. Soriano, E. Bandiello, L. Camacho, M. K. Nazeeruddin and H. J. Bolink, *Adv. Energy Mater.*, 2014, **4**, 1400345.
160 J. Kim, G. Kim, T. K. Kim, S. Kwon, H. Back, J. Lee, S. H. Lee, H. Kang and K. Lee, *J. Mater. Chem. A*, 2014, **2**, 17291–17296.
161 C. J. Brabec, S. E. Shaheen, C. Winder, N. S. Sariciftci and P. Denk, *Appl. Phys. Lett.*, 2002, **80**, 1288.
162 K.-G. Lim, M.-R. Choi, J.-H. Kim, D. H. Kim, G. H. Jung, Y. Park, J.-L. Lee and T.-W. Lee, *ChemSusChem*, 2014, **7**, 1125–1132.
163 S. K. M. J. and E. C. and F. Z. and W. R. S. and M. Fahlman, *Jpn. J. Appl. Phys.*, 2005, **44**, 3695.
164 K.-G. Lim, M.-R. Choi, H.-B. Kim, J. H. Park and T.-W. Lee, *J. Mater. Chem.*, 2012, **22**, 25148–25153.
165 T. Leijtens, I.-K. Ding, T. Giovenzana, J. T. Bloking, M. D. McGehee and A. Sellinger, *ACS Nano*, 2012, **6**, 1455–1462.
166 T. Leijtens, J. Lim, J. Teuscher, T. Park and H. J. Snaith, *Adv. Mater.*, 2013, **25**, 3227–3233.
167 J. Burschka, A. Dualeh, F. Kessler, E. Baranoff, N.-L. Cevey-Ha, C. Yi, M. K. Nazeeruddin and M. Grätzel, *J. Am. Chem. Soc.*, 2011, **133**, 18042–18045.
168 J. H. Noh, N. J. Jeon, Y. C. Choi, M. K. Nazeeruddin, M. Gratzel and S. Il Seok, *J. Mater. Chem. A*, 2013, **1**, 11842–11847.
169 H. Zhang, Y. Shi, F. Yan, L. Wang, K. Wang, Y. Xing, Q. Dong and T. Ma, *Chem. Commun.*, 2014, **50**, 5020–5022.
170 Y. S. Kwon, J. Lim, H.-J. Yun, Y.-H. Kim and T. Park, *Energy Environ. Sci.*, 2014, **7**, 1454–1460.

171 J. Liu, Y. Wu, C. Qin, X. Yang, T. Yasuda, A. Islam, K. Zhang, W. Peng, W. Chen and L. Han, *Energy Environ. Sci.*, 2014, **7**, 2963–2967.
172 Q. Wang, C. Bi and J. Huang, *Nano Energy*, 2015, **15**, 275–280.
173 J. M. Lee, J. S. Park, S. H. Lee, H. Kim, S. Yoo and S. O. Kim, *Adv. Mater.*, 2011, **23**, 629–633.
174 J. Lee, H. Kang, J.-Y. Hwang, S. W. Kim and S. Baik, *Carbon*, 2014, **79**, 337–345.
175 X. Dang, H. Yi, M.-H. Ham, J. Qi, D. S. Yun, R. Ladewski, M. S. Strano, P. T. Hammond and A. M. Belcher, *Nat. Nanotechnol.*, 2011, **6**, 377–384.
176 E. L. Unger, E. T. Hoke, C. D. Bailie, W. H. Nguyen, A. R. Bowring, T. Heumuller, M. G. Christoforo and M. D. McGehee, *Energy Environ. Sci.*, 2014, **7**, 3690–3698.
177 H. Nagaoka, F. Ma, D. W. deQuilettes, S. M. Vorpahl, M. S. Glaz, A. E. Colbert, M. E. Ziffer and D. S. Ginger, *J. Phys. Chem. Lett.*, 2015, **6**, 669–675.
178 H. J. Snaith, A. Abate, J. M. Ball, G. E. Eperon, T. Leijtens, N. K. Noel, S. D. Stranks, J. T.-W. Wang, K. Wojciechowski and W. Zhang, *J. Phys. Chem. Lett.*, 2014, **5**, 1511–1515.
179 J. Xu, A. Buin, A. H. Ip, W. Li, O. Voznyy, R. Comin, M. Yuan, S. Jeon, Z. Ning, J. J. McDowell, P. Kanjanaboos, J.-P. Sun, X. Lan, L. N. Quan, D. H. Kim, I. G. Hill, P. Maksymovych and E. H. Sargent, *Nat. Commun.*, 2015, **6**, 7081.
180 G. Xing, B. Wu, S. Chen, J. Chua, N. Yantara, S. Mhaisalkar, N. Mathews and T. C. Sum, *Small*, 2015, DOI: 10.1002/smll.201403719.
181 S. N. Habisreutinger, T. Leijtens, G. E. Eperon, S. D. Stranks, R. J. Nicholas and H. J. Snaith, *Nano Lett.*, 2014, **14**, 5561–5568.
182 G. Niu, W. Li, F. Meng, L. Wang, H. Dong and Y. Qiu, *J. Mater. Chem. A*, 2014, **2**, 705–710.
183 Y. Han, S. Meyer, Y. Dkhissi, K. Weber, J. M. Pringle, U. Bach, L. Spiccia and Y.-B. Cheng, *J. Mater. Chem. A*, 2015, **3**, 8139–8147.
184 B. J. Kim, D. H. Kim, Y.-Y. Lee, H.-W. Shin, G. S. Han, J. S. Hong, K. Mahmood, T. K. Ahn, Y.-C. Joo, K. S. Hong, N.-G. Park, S. Lee and H. S. Jung, *Energy Environ. Sci.*, 2015, **8**, 916–921.
185 K. Poorkazem, D. Liu and T. L. Kelly, *J. Mater. Chem. A*, 2015, **3**, 9241–9248.
186 C. Roldan-Carmona, O. Malinkiewicz, A. Soriano, G. Minguez Espallargas, A. Garcia, P. Reinecke, T. Kroyer, M. I. Dar, M. K. Nazeeruddin and H. J. Bolink, *Energy Environ. Sci.*, 2014, **7**, 994–997.
187 M. Dianetti, F. Di Giacomo, G. Polino, C. Ciceroni, A. Liscio, A. D'Epifanio, S. Licoccia, T. M. Brown, A. Di Carlo and F. Brunetti, *Sol. Energy Mater. Sol. Cells*, 2015, **140**, 150–157.
188 H. Kim, S.-H. Bae, T.-H. Han, K.-G. Lim, J.-H. Ahn and T.-W. Lee, *Nanotechnology*, 2014, **25**, 014012.
189 T.-H. Han, Y. Lee, M.-R. Choi, S.-H. Woo, S.-H. Bae, B. H. Hong, J.-H. Ahn and T.-W. Lee, *Nat. Photonics*, 2012, **6**, 105–110.
190 S. J. Lee, Y.-H. Kim, J. K. Kim, H. Baik, J. H. Park, J. Lee, J. Nam, J. H. Park, T.-W. Lee, G.-R. Yi and J. H. Cho, *Nanoscale*, 2014, **6**, 11828–11834.
191 J. T.-W. Wang, J. M. Ball, E. M. Barea, A. Abate, J. A. Alexander-Webber, J. Huang, M. Saliba, I. Mora-Sero, J. Bisquert, H. J. Snaith and R. J. Nicholas, *Nano Lett.*, 2014, **14**, 724–730.
192 J.-H. Im, I.-H. Jang, N. Pellet, M. Grätzel and N.-G. Park, *Nat. Nanotechnol.*, 2014, **9**, 927–932.
193 N. Kim, H. Kang, J.-H. Lee, S. Kee, S. H. Lee and K. Lee, *Adv. Mater.*, 2015, **27**, 2317–2323.
194 T.-W. Lee and Y. Chung, *Adv. Funct. Mater.*, 2008, **18**, 2246–2252.
195 M. R. Choi, T. H. Han, K. G. Lim, S. H. Woo, D. H. Huh and T. W. Lee, *Angew. Chemie - Int. Ed.*, 2011, **50**, 6274–6277.
196 S. Aharon, A. Dymshits, A. Rotem and L. Etgar, *J. Mater. Chem. A*, 2015, **3**, 9171–9178.